PHYSICAL REVIEW D **93,** 074025 (2016)

Pion-kaon scattering amplitude constrained with forward dispersion relations up to 1.6 GeV

J. R. Pelaez and A. Rodas

Departamento de Física Teórica II, Universidad Complutense de Madrid, 28040 Madrid, Spain

(Received 26 February 2016; published 20 April 2016)

In this work we provide simple and precise parametrizations of the existing πK scattering data from threshold up to 1.6 GeV, which are constrained to satisfy forward dispersion relations as well as three additional threshold sum rules. We also provide phenomenological values of the threshold parameters and of the resonance poles that appear in elastic scattering.

DOI: 10.1103/PhysRevD.93.074025

I. INTRODUCTION

Pion-kaon scattering is a very relevant process for our understanding of hadron physics and the strong interaction. The motivation to study it is threefold.

First of all, because pions and/or kaons appear in the final states of all hadronic processes. In particular kaons do so if the process involves net strangeness. Since pions and kaons interact strongly, final state πK rescattering effects are essential to describe and understand such hadronic processes.

Second, the reaction is interesting by itself, because even though we cannot solve QCD at low energies, the identification of pions and kaons as pseudo Goldstone bosons of the QCD spontaneous chiral symmetry breaking allows for a rigorous formulation in terms of a low-energy effective theory known as chiral perturbation theory (ChPT) [1]. In turn, ChPT provides πK scattering amplitudes which have been calculated first to one loop [2] and then to two loops [3]. Relevant constraints on the ChPT low-energy constants can be obtained from sum rules and dispersion relations applied to πK scattering [4]. In addition, πK scattering was subsequently unitarized to one loop [5,6] or within the chiral unitary approach [7], providing a simultaneous description of the low-energy and resonant regimes. Moreover, there is a renewed interest in πK scattering in lattice QCD, where the main features, like threshold parameters [8], scattering phases and resonances [9], have already been calculated. Although the pion mass used for these lattice calculations is not physical, one can expect physical values to be within reach soon. Alternative lattice strategies that calculate πK scattering from unitarized chiral Lagrangians have also been followed recently in [10].

Third, in pion-kaon scattering appear some of the still controversial light scalar mesons, like the $K_0^*(800)$ or κ resonance and the $K_0^*(1430)$. The former has been the subject of a long-standing debate about its very existence and nature. Actually, it is a firm candidate to form the lightest nonet of scalar mesons together with the $f_0(500)$ or σ meson, the $f_0(980)$ and the $a_0(980)$. There is strong evidence that these states might form a nonet of non-ordinary mesons [7,11], i.e., mesons not predominantly made of a quark and an antiquark. The κ resonance has been obtained within different variants of unitarized ChPT in [6,7]. It has also been shown to have a mass smaller than 900 MeV [12] and has been found [13] from a rigorous *solution* [14] of the Roy-Steiner dispersion relations [15], which is the best determination so far. However, those pieces of evidence are still not considered enough by the Review of Particle Physics (RPP) [16], which still lists the $K_0^*(800)$ resonance under the "needs confirmation" label. Thus, the κ meson is a further motivation for our present study, since any rigorous resonance determination from data (not a solution of dispersion relations or lattice) requires first a consistent knowledge of πK scattering, which, in order to control all uncertainties, should reach beyond the pure elastic regime. Incidentally, the latter region is also of direct interest for the $K_0^*(1430)$ resonance.

Hence, the goal of this work is to perform an analysis of the existing πK scattering data constrained to satisfy forward dispersion relations. The advantage of these relations is that, contrary to other kinds of dispersion relations (like Roy-Steiner equations in their simplest form), they can be easily implemented up to arbitrarily high energies. Here we will apply to πK scattering an approach that has been recently followed [17] to obtain a precise description of $\pi\pi$ scattering data, consistent with dispersion relations. Namely, on a first stage one obtains simple fits to different, even conflicting, sets of data for each partial wave up to 1.74 GeV, without any further constraint apart from unitarity. The resulting parametrizations form a set of simple "unconstrained fits to data" that could be easily modified wave by wave in case new data would appear. However, we check later to see that this set is not consistent with forward dispersion relations up to 1.74 GeV. Then, using this set as a starting point, one refines its parameters by imposing the dispersion relations without spoiling the data description. The resulting "constrained fits to data" will be the main result of this work and will provide precise parametrizations describing

 © 2016 American Physical Society

the existing data, while being simultaneously consistent with forward dispersion relations up to 1.6 GeV as well as with three threshold sum rules. Since these parametrizations are rather simple, we expect that they will become a useful tool for further studies, either theoretical or experimental, involving πK scattering at some stage and particularly for the precise determination of resonance parameters. This was indeed the case of the parametrizations resulting from a similar analysis of $\pi\pi$ scattering.

II. KINEMATICS AND NOTATION

As is customary we will use the partial wave decomposition of the πK scattering amplitudes

$$T^I(s,t,u) = \frac{4}{\pi}\sum_l (2l+1)P_l(\cos\theta)t_l^I(s), \qquad (1)$$

where s, t, u are the standard Mandelstam variables, satisfying $s+t+u = 2(m_\pi^2+m_K^2)$ and $\sigma(s) = 2q_{K\pi}/\sqrt{s}$. The center of mass momentum of two particles with mass m_1 and m_2 is

$$q_{12}(s) = \frac{1}{2\sqrt{s}}\sqrt{(s-(m_1+m_2)^2)(s-(m_1-m_2)^2)}. \qquad (2)$$

For later convenience we also define $\Sigma_{12} = m_1^2+m_2^2$ and $\Delta_{12} = m_1^2-m_2^2$. Unless explicitly stated, $m_1 = m_K$ and $m_2 = m_\pi$ and $q = q_{K\pi}$ in this work. Note that we are working in the isospin limit of equal masses for all pions $m_\pi = 139.57$ MeV and equal masses for all kaons $m_K = 496$ MeV. We also use $m_\eta = 547$ MeV.

The elastic unitarity condition $\mathrm{Im}t(s) = \sigma(s)|t(s)|^2$ implies that the elastic partial wave can be recast in terms of a real phase shift

$$t_l(s) = \frac{\hat{t}(s)}{\sigma(s)} = \frac{e^{i\delta_l(s)}\sin\delta_l(s)}{\sigma(s)} = \frac{1}{\sigma(s)}\frac{1}{\cot\delta(s)-i}, \qquad (3)$$

where we have introduced the "Argand" partial wave $\hat{t}(s)$ for later convenience.

In contrast, in the inelastic regime an inelasticity function is also introduced to write

$$t_l(s) = \frac{\hat{t}(s)}{\sigma(s)} = \frac{\eta_l(s)e^{2i\delta_l(s)}-1}{2i\sigma(s)}. \qquad (4)$$

Later on we will also study the scattering at very low energies through the threshold parameters defined as

$$\mathrm{Re}\hat{t}_l^I(s) \sim q^{2l+1}(a_l^I + b_l^I q^2 + O(q^4)). \qquad (5)$$

Throughout this work we will also use the traditional spectroscopic notation, naming the partial waves with isospin I and angular momentum $l = 0,1,2,3\ldots$ as S^I, P^I, D^I and F^I waves …, respectively.

III. UNCONSTRAINED FITS TO DATA

A. The data

Data on πK scattering were obtained mostly during the 1970s and the 1980s, measured indirectly from $KN \to K\pi N$ reactions, assuming they are dominated by the exchange of a single pion.

On the one hand, data on the $I = 3/2$ πK scattering cross sections was isolated in the early 1970s using different reactions: early experiments provided cross sections by studying $K^-d \to K^-\pi^- pp$ in Cho *et al.* [18] and $K^-n \to K^-\pi^- p$ in Bakker *et al.* [19] as well as $K^\pm p \to K^\pm\pi^-\Delta^{++}$ in Jongejans *et al.* [20]. Since this πK channel seems elastic up to at least 1.8 GeV, it is straightforward to obtain the phase shift. Actually, this was done explicitly by Linglin *et al.* in [21] from their $K^-p \to K^-\pi^-\Delta^{++}$ analysis. In general, the experiments in the earlier 1970s have low statistics, which were improved by later experiments. In particular, in 1977 Estabrooks *et al.* [22] performed a relatively high statistics analysis of $K^\pm p \to K^\pm\pi^+ n$ and $K^\pm p \to K^\pm\pi^-\Delta^{++}$ at 13 GeV to obtain the $I = 3/2$ πK component, also with no evidence of inelasticity up to 1.8 GeV in πK scattering. We will see that the differences between experiments are larger than the statistical uncertainties they quote, which points to the existence of a sizable systematic uncertainty that we will have to estimate separately for each wave.

On the other hand, isospin $I = 1/2$ scattering waves have always been obtained in combination with those with $I = 3/2$. This was done for instance by Mercer *et al.* in [23] using the $K^+p \to K^+\pi^-\Delta^{++}$ and $K^+p \to K^0\pi^0\Delta^{++}$ reactions. Due to low statistics, in order to separate different isospins, they needed to combine their results with the so-called world data summary tape, a heterogeneous and not very precise collection of data that existed at that time. As a consequence, the results for their $I = 1/2$ and $3/2$ waves have huge uncertainties, which is why they are usually neglected against later and more precise experiments.

As a matter of fact, what was really measured in scattering experiments was the $t_l = t_l^{1/2} + t_l^{3/2}/2$ combination. This was already studied with relatively high statistics in [22] up to 1.85 GeV, but also in the experiment with the highest statistics so far that was performed in the 1980s by Aston *et al.* at the LASS spectrometer [24] at SLAC. This LASS experiment studied the $K^-p \to K^-\pi^+ n$ reaction at 11 GeV and obtained the same πK partial wave combination up to 2.6 GeV.

The analysis needed to extract πK scattering amplitudes from $KN \to K\pi N$ has several sources of systematic uncertainties, like corrections to the on-shell extrapolation of the exchanged pion or rescattering effects. However, most experimental works only quote statistical uncertainties for

each solution and for this reason conflicting data exist. This will be clearly seen in the figures below. Thus, in our fits we sometimes add a systematic uncertainty to different sets or to certain data points which are in conflict with other data points in the same region. In the case of the most delicate and controversial wave, which is the $S^{1/2}$, we have checked to see that the resulting data set and the fit are consistent with certain statistical tests explained in Appendix B.

In addition some ambiguities occur in the determination of the phase that sometimes lead to different solutions for πK scattering even within the same $KN \to K\pi N$ experiment. In the case of Aston *et al.* [24] these ambiguities appear above the region of interest for this work. In contrast, Estabrooks *et al.* [22] do have four solutions above 1.5 GeV, but we only consider solution B since it is the one qualitatively closer to Aston *et al.*

So far we have been discussing scattering data where the $I = 1/2$ state has always been obtained in combination with the $I = 3/2$ one. However, it is also possible to obtain information on πK scattering from the decays of heavier particles. In particular, when πK's are the only strongly interacting particles in the decay, the Watson theorem implies that, in the πK elastic region, the phase of the global process should be the same as the scattering phase shift. In particular, the phase-shift difference between S and P waves with $I = 1/2$ have been measured from $D^+ \to K^-\pi^+e^+\nu_e$ by the *BABAR* Collaboration [25] and recently by the BESIII Collaboration [26]. The results are very consistent with the LASS experiment, but their uncertainties are too large and will not be included in our fits, although we will show them for completeness.

Moreover, there are measurements of the $I = 1/2$ phase of the $K\pi S$-wave amplitude obtained from Dalitz plot analyses of $D^+ \to K^-\pi^+\pi^+$ by the E791 [27], FOCUS [28] and CLEO-c [29] collaborations, as well as a recent similar analysis of $\eta_c \to K\bar{K}\pi$ by the *BABAR* Collaboration [30]. These phases (and amplitudes) are not necessarily those of πK scattering due to the presence of a third strongly interacting particle, which invalidates the use of Watson's theorem. However, *a posteriori* comparison with the scattering data has shown that, within the large uncertainties and at least in the elastic region, the resulting phase (but not the amplitude) is very similar to that of LASS. This means that the effect of the third particle on the phase is rather constant and almost amounts to a global shift. But these data cannot really be interpreted as a scattering phase beyond this qualitative agreement and are therefore not included in our fits. Nevertheless we will show and discuss them in comparison with our results.

B. General form of our parametrizations

Each partial wave will now be fitted to the existing data up to ~1.7 GeV, which means that we will only fit S, P, D and F waves, since there are no data for G, H and higher waves below 1.8 GeV. In this first stage, the fit to a wave with a given angular momentum will be performed independently of other waves with different angular momentum, by means of simple functions, without imposing any dispersive constraint. For this reason the resulting set of partial waves will be called an unconstrained fit to data (UFD). When possible, as in waves which are elastic in the whole energy range, a single functional form will be used throughout the whole energy region. However, for more complicated waves different functional forms will be used in different regions. Typically these piecewise functions will be matched at thresholds demanding continuity.

We would like to add a word of caution here. The data are not precise nor numerous enough to exclude large fluctuations between successive data points, particularly in certain energy regions. One could devise complicated parametrizations that would pass through every single data point, or even produce fluctuations between points. In this work we are assuming that such fluctuations do not occur and that the data can be correctly fitted with simple and relatively smooth parametrizations. The size of the uncertainties thus depends on this assumption. The parametrizations we describe below are the ones we have finally chosen because they satisfy the above assumption and yield uncertainty bands which do not show wild fluctuations or become too large in a region where the data spread does not require so. In particular, we have explored different kinds of conformal parametrizations (with different centers and more terms in the expansion, see Appendix A), we have tried simple polynomials in different variables, including orthogonal polynomials in a given region, adding or removing resonant shapes, etc. Since all of them fit the data, their central result is not too different from our final choice. Except in a few relevant cases, we spare the reader from explaining the caveats that affect the many other parametrizations we tried. We just present below our final choice. Moreover, for a given parametrization, and once the systematic uncertainty that affects the data has been estimated, we decide to stop adding parameters when the χ^2/dof is close to or less than one. Of course, the size of the final uncertainties depends on our educated guess of systematic uncertainties, which, as we will see, dominate the final error bands in many cases.

1. Partial waves in elastic regions

For the elastic regions, in which a partial wave can be recast in terms of just a phase shift, we will use a conformal expansion of the type

$$\cot\delta_l(s) = \frac{\sqrt{s}}{2q^{2l+1}}F(s)\sum_n B_n\omega(s)^n, \tag{6}$$

where $F(s) = 1$ except for scalar waves that have an Adler zero at $s_{\rm Adler}$, in which case $F(s) = 1/(s - s_{\rm Adler})$, or for waves that exhibit a clear narrow resonance and whose phase shift crosses $\pi/2$ at m_r, in which case

$F(s) = (s - m_r^2)$. In addition, the conformal variable is defined as

$$\omega(y) = \frac{\sqrt{y} - \alpha\sqrt{y_0 - y}}{\sqrt{y} + \alpha\sqrt{y_0 - y}}, \quad y(s) = \left(\frac{s - \Delta_{K\pi}}{s + \Delta_{K\pi}}\right)^2. \quad (7)$$

This change of variables, which maps the complex s plane into the unit circle, is relatively similar to those used for $\pi\pi$ scattering in [17] or πK scattering in [12], and is explained in detail in Appendix A. It suffices here to say that, by taking full advantage of the analytic properties of the partial waves in the complex plane, such a conformal expansion ensures a rapid convergence of the series and no more than three B_i coefficients are needed for the fits to each wave in the elastic region. The $y_0 \equiv y(s_0)$ and α constants are fixed, not fitted, for each partial wave. The s_0 parameter sets the maximum energy at which this mapping is applicable on the real axis, whereas α fixes the energy where the expansion is centered.

2. Partial waves in inelastic regions

The parametrizations of partial waves in the inelastic region have to accommodate several resonant structures that have been observed and ensure a continuous matching with the elastic parametrization. Note that for the $D^{1/2}$ and $F^{1/2}$ waves, since data only exist in the inelastic region, we will use a unified inelastic formalism in the whole energy region, which reduces to the elastic case below the $K\eta$ threshold.

We have tried different parametrizations, like polynomial fits in powers of the πK, $K\eta$ momenta, or the s or $\sqrt{s}$ variables. However such fits tend to have small uncertainties close to the elastic region and very large as the energy increases, which does not necessarily reproduce the uncertainty observed in the data and leads to huge correlations. As other authors before [14], we have found that it is more efficient to describe this region with products of exponential or rational functions, which are more flexible to accommodate resonant structures and whose resulting uncertainty bands are more uniform throughout the fit region. Moreover, the use of products of functions allows for a straightforward implementation of unitarity, which is done as follows:

$$t_l(s) = \frac{1}{2i\sigma(s)}\left(\prod_n S_n(s) - 1\right). \quad (8)$$

The S_n could either have the form of a nonresonant background

$$S_n = S_n^b = \exp\left[2iq_{ij}^{2l+1}(\phi_0 + \phi_1 q_{ij}^2 + \cdots)\right], \quad (9)$$

with ϕ_k real parameters, or a resonantlike form

$$S_n = S_n^r = \frac{s_{rn} - s + i(P_n(s) - Q_n(s))}{s_{rn} - s - i(P_n(s) + Q_n(s))}, \quad (10)$$

where s_{rn} are real parameters and $P_n(s)$ and $Q_n(s)$ are polynomials that have the same sign over the inelastic region. Using the equations above, $|S_n| \leq 1$ and inelastic unitarity is satisfied. If these polynomials were constant, one would recover the simplest Breit-Wigner formula for S_n^r. We will explain in the following subsections the choice of polynomials for different waves. Continuity with the elastic region is imposed by fixing the $P_n(s)$ polynomial of the S_n that has a pole with the lowest s_{rn}. This formalism is a modification of the parametrizations used in [14] for the high energy region [31]. When reducing this parametrization to the elastic case, Q_n is set to zero, which as commented above is of relevance for the $D^{1/2}$ and $F^{1/2}$ waves.

Note that close to a resonance, each of the S_n^r functions bear some resemblance to a Breit-Wigner form, but the actual parameters of a resonance have to be calculated with the full partial wave and not obtained from an individual S_n^r. Let us remark once again that when combining the S_n's in the complete functional form of t_l, unitarity has been enforced exactly. This would not occur in a simple sum of Breit-Wigner amplitudes, which would violate unitarity.

We will use partial waves to describe data up to ~1.7 GeV. Beyond that energy we will use Regge theory to describe the amplitudes, as we will see in Sec. III G below.

C. S waves

1. $I = 3/2$ S wave

Let us then start by describing our simple fit to the $I = 3/2$ S wave, since data for this wave exist independently of other waves. Once again, we emphasize that there is no evidence so far of inelasticity up to ~1.8 GeV, and thus we will consider this wave as elastic up to that energy. Hence, as commented above and explained in more detail in the Appendix A, we will use the following simple functional form to describe the phase shift:

$$\cot\delta_0^{3/2}(s) = \frac{\sqrt{s}}{2q(s_{\rm Adler} - s)}(B_0 + B_1\omega(s) + B_2\omega(s)^2). \quad (11)$$

Note that we have explicitly factorized the Adler zero, which we will set to its leading order within chiral perturbation theory, i.e., $s_{\rm Adler} = \Sigma_{K\pi}$. For this wave, the constants that define the conformal variable ω in Eq. (7) are fixed to

$$\alpha = 1.4, \qquad s_0 = (1.84\ \text{GeV})^2. \quad (12)$$

The existing data are shown in Fig. 1. There is a relatively fair agreement between different experiments

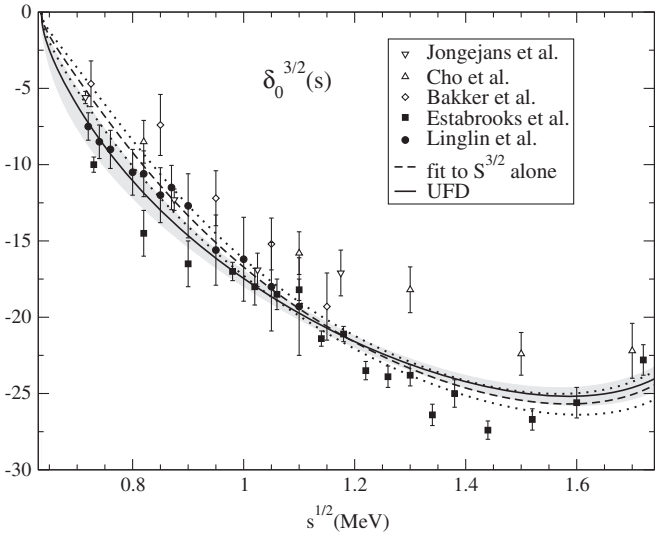

FIG. 1. Experimental data on the $S^{3/2}$ phase shift, $\delta_0^{3/2}(s)$. The data come from [18] (Cho *et al.*), [19] (Bakker *et al.*), [20] (Jongejans *et al.*), [21] (Linglin *et al.*) and [22] (Estabrooks *et al.*). The dashed line shows our fit to these data and the dotted lines enclose its uncertainty band. The continuous line represents our unconstrained fit including also the data on $t_0^{1/2}+t_0^{3/2}/2$, whose uncertainty is represented by the gray band.

below 1.1 GeV. However we can already notice some incompatible points between the Bakker *et al.* [19] and Estabrooks *et al.* [22] data sets, mostly due to the very small uncertainty of some points in the latter set. Note also the large variations between the uncertainties of successive data points in the Estabrooks *et al.* set. Above 1.1 GeV the two data sets that exist are largely incompatible. It is clear that some systematic uncertainty exists.

Therefore, we have fitted the data in Fig. 1 in two ways, either adding a constant systematic uncertainty of 1° or multiplying the existing statistical uncertainties by a factor of 2, which is chosen so that the resulting χ^2/d.o.f. is slightly less than one. The resulting fits are rather similar, but we have preferred the uncertainty band of the first because the systematic uncertainty is not correlated to the statistical one. In addition, the second approach satisfies much worse the threshold sum rules that we will check in the next sections. The result of our fit, with the estimate of systematic uncertainty added to the statistical uncertainties, is $\chi^2/\text{d.o.f.} = 37/(44-3+1)$.

Had we considered only two B_k parameters, the fit would yield an 80% larger χ^2/d.o.f, whereas with four it would decrease by 15%. Since three parameters as in Eq. (11) already provide a $\chi^2/\text{d.o.f.} < 1$, we do not consider it necessary to have a fourth parameter. We show this fit as a dashed line in Fig. 1, where the uncertainty band is delimited by the dotted lines.

Still this is not our final fit because there is also experimental information on the $t_S \equiv t_0^{1/2}+t_0^{3/2}/2$ combination. In the next subsection we will explain how the fit to the t_S data produces a small modification on the $S^{3/2}$ wave. The result provides the final $S^{3/2}$ parametrization, which is also shown in Fig. 1 as a thick continuous line whose uncertainties are covered by the gray band. Since no dispersion relation has been imposed yet, this result will be called an UFD, whose parameters are found in Table I. The constrained fit to data (CFD) in that table will be discussed later in Sec. V. In the figure it can be noticed that this UFD result is similar to the fit to the $S^{3/2}$-wave data alone that has been described in this subsection.

TABLE I. Parameters of the $S^{3/2}$ wave.

Parameter	UFD	CFD
B_0	2.25 ± 0.04	2.27 ± 0.04
B_1	4.21 ± 0.17	3.94 ± 0.17
B_2	2.45 ± 0.50	3.36 ± 0.50

2. $I = 1/2$ S wave

For this wave, inelasticity has been measured above 1.3 GeV and for the most part it is due to the $K\eta$ state rather than to states with more than two mesons. Hence, we are going to parametrize the amplitude using the elastic formalism of Sec. III B 1 below the $K\eta$ threshold, and with the inelastic formalism of Sec. III B 2 above that threshold.

Thus, for $(m_K+m_\pi)^2 \le s \le (m_K+m_\eta)^2$ we will use a conformal expansion of the type in Eq. (6), namely,

$$\cot\delta_0^{1/2}(s) = \frac{\sqrt{s}}{2q(s-s_{\text{Adler}})}(B_0+B_1\omega). \tag{13}$$

Once again we have explicitly factorized the Adler zero, which we have set to its leading order within chiral perturbation theory value:

$$s_{\text{Adler}} = \left(\Sigma_{K\pi}+2\sqrt{\Delta_{K\pi}^2+m_K^2m_\pi^2}\right)/5 \simeq 0.236\ \text{GeV}^2. \tag{14}$$

As explained in Appendix A, for this wave it is convenient to fix the constants that define the center of the conformal variable ω in Eq. (7) to the following values:

$$\alpha = 1.15, \qquad s_0 = (1.1\ \text{GeV})^2. \tag{15}$$

The parameters obtained for the best UFD are given in the first column of Table II.

TABLE II. Parameters of the elastic $S^{1/2}$ wave.

Parameter	UFD	CFD
B_0	0.411 ± 0.007	0.411 ± 0.007
B_1	0.181 ± 0.034	0.162 ± 0.034

In contrast, in the $s \geq (m_K + m_\eta)^2$ region we will implement the inelastic formalism of Eqs. (8), (9), (10) as follows:

$$t_0^{1/2}(s) = \frac{S_0^b S_1^r S_2^r - 1}{2i\sigma(s)}, \tag{16}$$

where

$$S_0^b = \exp[2iq_{\eta K}(\phi_0 + \phi_1 q_{\eta K}^2)]. \tag{17}$$

For S_1^r we use Eq. (10) with

$$P_1(s) = (s_{r1} - s)\beta + e_1 G_1 \frac{p_1(q_{\pi K})}{p_1(q_{\pi K}^r)} \frac{q_{\pi K} - \hat{q}_{\pi K}}{q_{\pi K}^r - \hat{q}_{\pi K}}, \tag{18}$$

$$Q_1(s) = (1 - e_1) G_1 \frac{p_1(q_{\pi K})}{p_1(q_{\pi K}^r)} \frac{q_{\eta K}}{q_{\eta K}^r} \Theta_{\eta K}(s), \tag{19}$$

where $p_1(x) = 1 + ax^2 + bx^4$, $q_{ij}^r = q_{ij}(s_r)$, $\hat{q}_{ij} = q_{ij}((m_\eta + m_K)^2)$ and $\Theta_{\eta K}(s) = \Theta(s - (m_K + m_\eta)^2)$ is the step function at the $K\eta$ threshold. In addition, for S_2^r we use Eq. (10) with

$$P_2(s) = e_2 G_2 \frac{p_2(q_{\pi K})}{p_2(q_{\pi K}^r)} \frac{q_{\pi K} - \hat{q}_{\pi K}}{q_{\pi K}^r - \hat{q}_{\pi K}}, \tag{20}$$

$$Q_2(s) = (1 - e_2) G_2 \frac{p_2(q_{\pi K})}{p_2(q_{\pi K}^r)} \frac{q_{\eta K}}{q_{\eta K}^r} \Theta_{\eta K}(s), \tag{21}$$

with $p_2(x) = 1 + cx^2$.

By matching the elastic and inelastic parametrizations at the $K\eta$ threshold we only need to demand continuity, which is ensured by defining $\beta \equiv 1/\cot\delta_0^{1/2}((m_K + m_\eta)^2)$, where $\delta_0^{1/2}$ is calculated here with the elastic parametrization in Eq. (13).

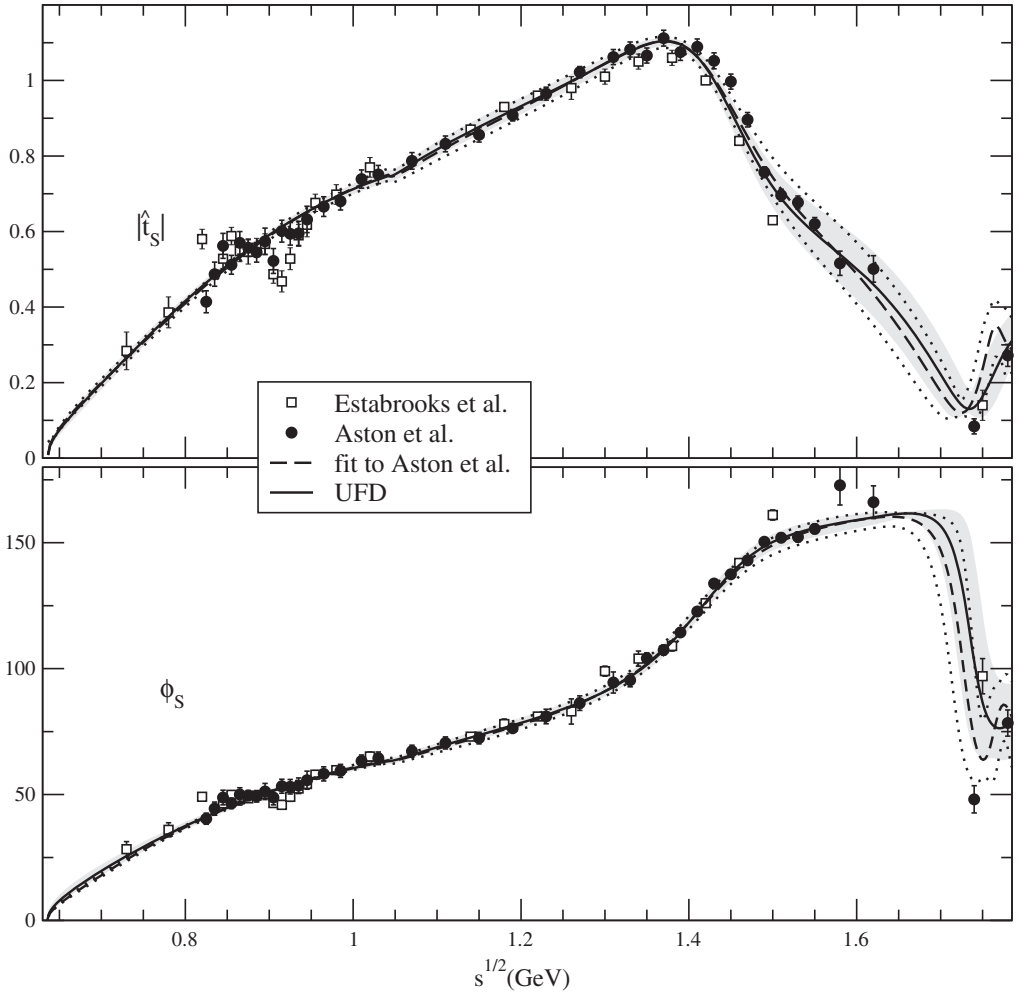

FIG. 2. Data on $\hat{t}_S(s)$ from Estabrooks *et al.* [22] and Aston *et al.* [24]. The upper panel shows $|\hat{t}_S(s)|$, whereas the lower one shows $\phi_S(s)$, which were measured independently. The continuous line is our unconstrained fit (UFD), whose uncertainties are covered by the gray band. For comparison we show, as a dashed line, a fit only to the data in [24], whose corresponding uncertainties are delimited by the dotted lines.

3. t_S wave

Nevertheless, as already explained above, we do not fit the $S^{1/2}$ wave alone, but in the $t_S \equiv t_0^{1/2} + t_0^{3/2}/2$ combination that was originally measured. Let us then define

$$t_S(s) = |t_S(s)|e^{i\phi_S(s)}, \tag{22}$$

and remark that, since $|t_S|$ and ϕ_S were measured independently, we will fit them both. In order to compare with data is convenient to use the normalization

$$\hat{t}_S(s) = t_S(s)\sigma(s). \tag{23}$$

Thus, in Fig. 2 we show the data on $\hat{t}_S$ and the result of our UFD. The upper panel shows $|\hat{t}_S|$, whereas the lower one shows ϕ_S. The combined χ^2/d.o.f. of the $S^{1/2}$ and $S^{3/2}$ data fits is $\chi^2/\text{d.o.f.} = 168/(182-15+1)$ with the UFD parameters provided in Table III. The e_1 parameter was initially left free but it comes out practically indistinguishable from 1, with tiny uncertainties, and has been fixed later to 1 for practical purposes.

From Fig. 2 it can be easily noted that there are data points which are largely incompatible with one another, not only between the two different experiments [22,24], but even among the successive data points of Estabrooks *et al.* [22]. Thus, it seems clear that there are some systematic errors not covered by the experimental uncertainties. Since these are the most controversial waves, here we have followed a more elaborate procedure to estimate the uncertainties of the resulting fit. In particular, we follow one of the techniques suggested in [32], which, in brief, consists of running Gaussianity tests on the data with respect to the fit and enlarge the uncertainties of those data points that spoil the test. This yields a new fit upon which the procedure is iterated until the Gaussianity test is satisfied. The details of this method are given in Appendix B. We show in Fig. 2, as a gray band, the resulting uncertainty of our fit to those data and the $I = 3/2$ data already discussed in the previous section.

TABLE III. Parameters of the $S^{1/2}$ inelastic fit.

Parameters	UFD	CFD
ϕ_0	-0.20 ± 0.04 GeV^{-1}	-0.19 ± 0.04 GeV^{-1}
ϕ_1	4.76 ± 0.25 GeV^{-3}	5.03 ± 0.25 GeV^{-3}
a	-5.22 ± 0.04 GeV^{-2}	-5.20 ± 0.04 GeV^{-2}
b	7.57 ± 0.13 GeV^{-4}	7.60 ± 0.13 GeV^{-4}
c	-1.72 ± 0.07 GeV^{-2}	-1.73 ± 0.07 GeV^{-2}
$\sqrt{s_{r1}}$	1.399 ± 0.006 GeV	1.401 ± 0.006 GeV
$\sqrt{s_{r2}}$	1.815 ± 0.017 GeV	1.817 ± 0.017 GeV
e_1	1	1
e_2	0.184 ± 0.033	0.184 ± 0.033
G_1	0.499 ± 0.017 GeV	0.497 ± 0.017 GeV
G_2	0.29 ± 0.12 GeV	0.28 ± 0.12 GeV

In the literature it is rather usual [14,33–35] to neglect the Estabrooks *et al.* data, although it is not always the case [36]. To be able to compare with this choice, we have thus considered a fit to the $I = 3/2$ data together with only the $I = 1/2$ data set of Aston *et al.* [24], which is much smoother than that of Estabrooks *et al.* [22], particularly below 1.5 GeV. In this case we have not added any systematic uncertainty and the result is shown in Fig. 2 as a dashed line, which almost overlaps with our previous fit up to 1.5 GeV, and has a very similar uncertainty band represented as the area between dotted lines. However, above 1.5 GeV and up to 1.7 GeV, the Aston *et al.* [24] set is not so consistent. For instance, it is well known that two of its points violate unitarity [36] (which we have always removed from our fits). Nevertheless, it is still compatible with our previous fit within uncertainties. Since here we want to stay on the conservative side, we have decided not to neglect the Estabrooks *et al.* data. Thus, from now on we will consider our UFD result only, which describes both sets. We will repeat this comparative exercise for other waves, but in all cases we will keep the UFD result obtained by fitting both sets when they exist.

With the combined fit to the $I = 1/2$ and $I = 3/2$ data we can separate the results for each isospin partial wave. The UFD result for the $I = 3/2$ S wave was already shown in its elastic region in Fig. 1, whereas we show now in Fig. 3 the resulting $I = 1/2$ S-wave phase shift. Note once

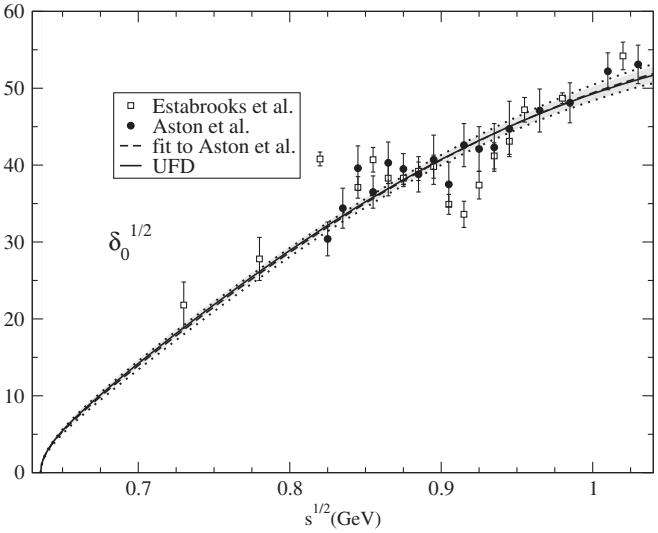

FIG. 3. $S^{1/2}$-wave phase shift below the $K\eta$ threshold. In this region the amplitude is elastic in practice. The continuous line is our UFD result, whose uncertainty is covered by the gray band. Data points extracted from Estabrooks *et al.* [22] and Aston *et al.* [24]. As explained in the text, we do not fit this wave individually, but in combination with the $I = 3/2$, as it was originally measured. The dashed curve is the fit to Aston *et al.* [24] data alone and the dotted lines cover the corresponding uncertainty band.

TABLE IV. S-wave scattering lengths from our UFD and CFD sets, in m_π^{-1} units, compared to other values in the literature.

	$m_\pi a_0^{1/2}$	$m_\pi a_0^{3/2}$
Büttiker *et al.*, Ref. [14]	0.224 ± 0.022	-0.0448 ± 0.0077
Dobado and Peláez, Ref. [37]	0.155 ± 0.012	-0.049 ± 0.004
Jamin *et al.*, Ref. [36]	0.18	-0.12
Bugg, Ref. [33]	0.195 ± 0.006	...
Zhou and Zheng, Ref. [34]	0.219 ± 0.034	-0.042 ± 0.002
UFD, this work	0.22 ± 0.01	$-0.10^{+0.03}_{-0.05}$
CFD, this work	$\mathbf{0.22 \pm 0.01}$	$\mathbf{-0.054^{+0.010}_{-0.014}}$

again that in the elastic region our UFD result is almost identical to the fit to Aston *et al.* data alone.

4. S-wave scattering lengths

Once we have fitted the data on the two S waves, we can use our UFD parametrizations to obtain the scattering lengths defined in Eq. (5), which we show in Table IV. Note that they are in fair agreement with other existing values in the literature, also provided in the table.

There is a renewed interest towards these quantities due to recent lattice calculations [8] and also due to the experimental measurement by the DIRAC Collaboration [38],

$$\frac{1}{3}(a_0^{1/2} - a_0^{3/2}) = 0.11^{+0.09}_{-0.04} m_\pi^{-1} \quad \text{(DIRAC)}, \tag{24}$$

which was not determined from scattering experiments, but from the formation of πK atoms. From our UFD set we find

$$\frac{1}{3}(a_0^{1/2} - a_0^{3/2}) = 0.108^{+0.018}_{-0.010} m_\pi^{-1} \quad \text{(UFD)}. \tag{25}$$

Note that our uncertainties are smaller, by roughly an order of magnitude, than the present direct experimental knowledge. We have explicitly checked to see that including the DIRAC value or not does not change the result of our fits.

D. P waves

1. $I = 3/2$ P wave

Only Estabrooks *et al.* [22] provide data for the $I = 3/2$ P-wave phase shift up to 1.74 GeV, which we show in Fig. 4. As can be noticed in the figure, this wave is rather small. Namely, below 1.1 GeV its phase shift is less than 1°, below 1.4 GeV it is less than 2° and below 1.74 GeV it is less than 3°. There is no inelasticity measured up to 1.74 GeV so that we will parametrize this partial wave with a conformal expansion as in Eqs. (6) and (7):

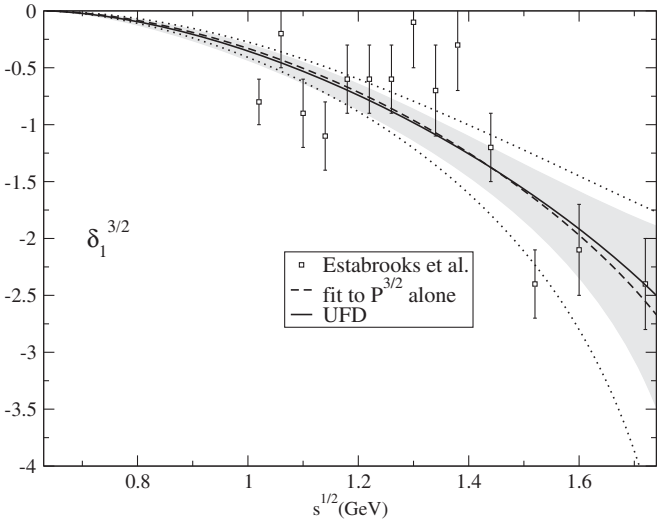

FIG. 4. Data on the $I = 3/2$ P wave from Estabrooks *et al.* [22]. We also show our UFD result as solid line with a gray uncertainty band, which is obtained by fitting these data together with the data on the $t_P = t_1^{1/2} + t_1^{3/2}/2$ combination. For comparison we show with a dashed line a fit only to the data in this figure, whose uncertainty is delimited by the dotted lines.

$$\cot \delta_1^{3/2}(s) = \frac{\sqrt{s}}{2q^3}(B_0 + B_1 \omega). \tag{26}$$

Let us remark that the α parameter that defines the conformal variable ω [see Eq. (7)] has been chosen so that the center of the conformal expansion lies on the center of the region where data exists. Thus, for this wave we have set

$$\alpha = 1.45, \qquad s_0 = (1.84\ \text{GeV})^2. \tag{27}$$

The existence of systematic uncertainties is evident from Fig. 4. If we make a naive fit without taking these systematic effects into account, the resulting $\chi^2/\text{d.o.f.} \simeq 2$. Hence, we have included an estimation of the systematic uncertainty in our fits by multiplying the data statistical uncertainties by $\sqrt{2}$. Two conformal parameters are enough to describe this wave and no significant improvement is obtained by considering a third one.

As happened with the $S^{3/2}$ wave, our final fit for the $I = 3/2$ P wave is obtained by fitting simultaneously the data for this wave alone together with the data on the $t_P \equiv t_1^{1/2} + t_1^{3/2}/2$ combination obtained by Estabrooks *et al.* [22] and Aston *et al.* [24]. The resulting UFD is shown in Fig. 4, where the gray band covers its uncertainty. The corresponding UFD parameters are listed in Table V.

Also in Fig. 4 we show, as a dashed line, the result when fitting only the data on that wave. Its corresponding uncertainty band is delimited by dotted lines. As we can

TABLE V. Parameters of the $P^{3/2}$ wave.

Parameter	UFD	CFD
B_0	-14.8 ± 2.6	-15.6 ± 2.6
B_1	2.7 ± 7.4	-2.2 ± 7.4

see, it is almost indistinguishable from our UFD result, for which we have also fitted data on $t_P \equiv t_1^{1/2} + t_1^{3/2}/2$, as we will see next.

2. $I = 1/2$ P wave

The $I = 1/2$ wave is only measured in scattering experiments together with the $I = 3/2$ wave in the t_P combination defined just above. Although in the literature it is frequent to neglect the $P^{3/2}$ wave, because as we have just seen it is very small, we will keep it in our fits for completeness.

Let us then discuss the $P^{1/2}$ wave in the elastic region, i.e., $s \leq (m_\eta + m_K)^2$, for which we use a conformal fit to describe the data, namely,

$$\cot\delta_1^{1/2}(s) = \frac{\sqrt{s}}{2q^3}(m_r^2 - s)(B_0 + B_1\omega + B_2\omega^2). \quad (28)$$

Note that we have explicitly extracted an $(m_r^2 - s)$ factor so that the phase crosses $\pi/2$ at the energy of the peak associated with the $K^*(892)$ resonance, which is the dominant feature of this wave in the elastic region. As explained in Appendix A, the α and s_0 parameters, which define the conformal variable ω in Eq. (7), are fixed from the choice of the center of the expansion and the highest energy of the fit to be

$$\alpha = 1.15, \qquad s_0 = (1.1\ \text{GeV})^2. \quad (29)$$

For $s \geq (m_\eta + m_K)^2$, we will use once more the inelastic formalism of Eqs. (8) and (10). Thus, we write

$$t_1^{1/2}(s) = \frac{S_1^r S_2^r S_3^r - 1}{2i\sigma(s)}, \quad (30)$$

where all the S_k^r's are of the form in Eq. (10), with

$$P_1 = (s_{r1} - s)\beta + e_1 G_1 \frac{p_1(q_{\pi K})}{p_1(q_{\pi K}^r)} \frac{q_{\pi K}^2 - \hat{q}_{\pi K}^2}{(q_{\pi K}^r)^2 - \hat{q}_{\pi K}^2} \frac{q_{\pi K}}{q_{\pi K}^r},$$

$$P_{2,3} = e_{2,3} G_{2,3} \frac{p_{2,3}(q_{\pi K})}{p_{2,3}(q_{\pi K}^r)} \frac{q_{\pi K}^2 - \hat{q}_{\pi K}^2}{(q_{\pi K}^r)^2 - \hat{q}_{\pi K}^2} \frac{q_{\pi K}}{q_{\pi K}^r},$$

$$Q_{1,2,3} = (1 - e_{1,2,3}) G_{1,2,3} \frac{p_{1,2,3}(q_{\pi K})}{p_{1,2,3}(q_{\pi K}^r)} \left(\frac{q_{\eta K}}{q_{\eta K}^r}\right)^3 \Theta_{\eta K}(s). \quad (31)$$

In addition,

$$p_i(q_{\pi K}) = 1 + a_i q_{\pi K}^2, \quad (32)$$

and $\Theta_{\eta K}(s) = \Theta(s - (m_K + m_\eta)^2)$ is the step function at the $K\eta$ threshold. Again, in order to impose continuity at $K\eta$ threshold we have defined $\beta \equiv 1/\cot\delta_1^{1/2}((m_K + m_\eta)^2)$, with $\delta_1^{1/2}$ calculated from the elastic expression in Eq. (28).

3. t_P wave

Thus, now that we have the functional forms for the $I = 1/2$ and $I = 3/2$ P waves, we can perform the fit to all the P-wave data. As we did for the S wave we first define

$$t_P(s) = |t_P(s)| e^{i\phi_P(s)}, \quad (33)$$

which is sometimes used with the alternative normalization

$$\hat{t}_P(s) = t_P(s)\sigma(s). \quad (34)$$

As commented before, we fit simultaneously the $I = 3/2$ data in Fig. 4 and the data on both $|\hat{t}_P|$ and ϕ_P that we show in Figs. 5 and 6. Note that once again there are clear systematic deviations of certain points, particularly from the Estabrooks *et al.* data set [22]. In this case we have proceeded as follows: we have performed a first fit, then we have added a systematic uncertainty to the isolated incompatible data points, which is half of their distance to the central value of the fit. In regions where the two sets of data are incompatible a systematic uncertainty is also added to each set, which corresponds to half of the average

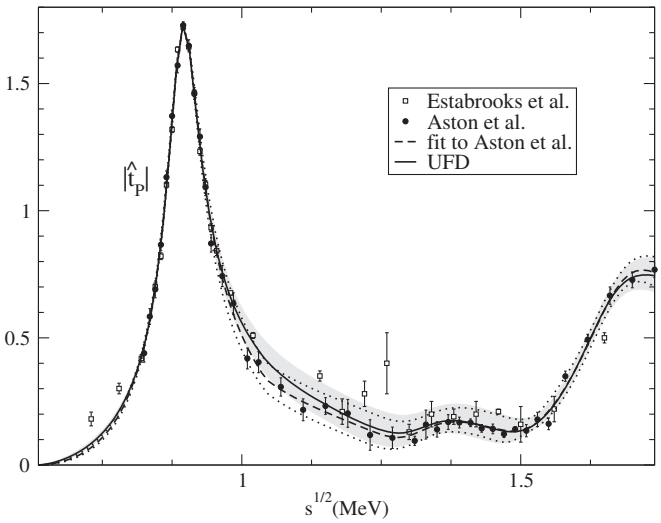

FIG. 5. Data on $|\hat{t}_P(s)|$ from [22,24]. The continuous line is our unconstrained fit (UFD), whose uncertainties are covered by the gray band. For comparison we show as a dashed line a fit only to the data from [24], whose corresponding uncertainties are delimited by the dotted lines.

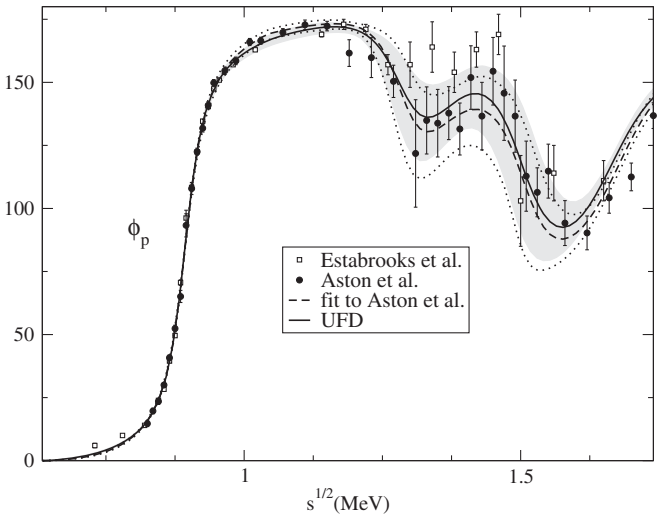

FIG. 6. Data on $\phi_P(s)$ from Estabrooks *et al.* [22] and Aston *et al.* [24]. The continuous line is our unconstrained fit (UFD), whose uncertainties are covered by the gray band. For comparison we show as a dashed line a fit only to the data from [24], whose corresponding uncertainties are delimited by the dotted lines.

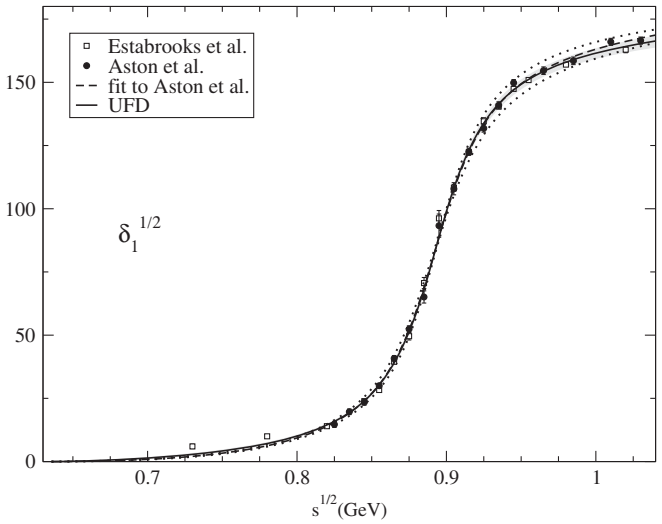

FIG. 7. $P^{1/2}$-wave phase shift below the $K\eta$ threshold. The continuous line is our UFD parametrization, whose uncertainty is covered by the gray band. Data from Estabrooks *et al.* [22] and Aston *et al.* [24]. The dashed curve is the fit to Aston *et al.* data alone and the dotted lines cover its corresponding uncertainty.

difference from the fit to the data set in that region. With these additional systematic uncertainties we have performed a final fit, which we call an UFD, with $\chi^2/\text{d.o.f.} = 76.4/(78-12+1)$. The resulting curves are also shown in Figs. 5 and 6, together with a fit in which we have only fitted the Aston *et al.* data for the $I=1/2$ wave. It can be noticed that in such a case the result would still be compatible with our UFD.

Once all P-wave data have been fitted, we can separate the different isospin components. The $I=3/2$ UFD result was already discussed in Sec. III D 1 and its parameters were given in Table V.

Concerning the $P^{1/2}$ wave, let us first look at the elastic region. When restricted below the $K\eta$ threshold the UFD result has $\chi^2/\text{d.o.f.} = 27/(34-4+1)$ and the corresponding parameters are listed in Table VI. The resulting curve for the $P^{1/2}$ wave can be seen in Fig. 7, where the distinct shape of the $K^*(892)$ is nicely observed. We are also showing a fit where only the data of Aston *et al.* has been fitted and how the results are hard to distinguish from our UFD line, except for the somewhat larger uncertainty band of the latter, particularly at higher energies.

The UFD parameters for the $P^{1/2}$-wave inelastic parametrization are given in Table VII. Note that to describe the inelastic region we still need to take into account the high energy tail of the $K^*(892)$ resonance, which is elastic, so that we set $e_1=1$. In addition its mass is fixed to the neutral case, 896 MeV, since this is the one measured in the LASS [24] and Estabrooks *et al.* [22] experiments. The other resonance shapes of the $K^*(1410)$ and $K^*(1680)$ are also very nicely described.

Let us remark that there is a recent fit to the t_P data [39], neglecting the $I=3/2$ wave as usual, in which the authors also consider three poles for the $I=1/2$ partial wave within a two-channel K-matrix approach, the channels being πK and $\pi K^*(892)$. In [39] only the central value of the fit is given and, since it is a fit to basically the same data we fit here, the results are relatively similar to ours within uncertainties—actually, around 1 GeV it is slightly closer to our CFD result, which we will discuss later on,

TABLE VI. $P^{1/2}$-wave parameters in the elastic region.

Parameter	UFD	CFD
B_0	0.97 ± 0.02	0.97 ± 0.02
B_1	0.98 ± 0.30	0.55 ± 0.30
B_2	0.79 ± 0.95	0.75 ± 0.95
m_r	0.8957 ± 0.0004 GeV	0.8957 ± 0.0004 GeV

TABLE VII. $P^{1/2}$-wave parameters in the inelastic region.

Parameters	UFD	CFD
a_1	-1.90 ± 0.10 GeV^{-2}	-1.76 ± 0.10 GeV^{-2}
a_2	-2.14 ± 0.23 GeV^{-2}	-2.33 ± 0.23 GeV^{-2}
a_3	-1.34 ± 0.07 GeV^{-2}	-1.41 ± 0.07 GeV^{-2}
$\sqrt{s_{r1}}$	0.896 GeV (fixed)	0.896 GeV (fixed)
$\sqrt{s_{r2}}$	1.346 ± 0.012 GeV	1.347 ± 0.012 GeV
$\sqrt{s_{r3}}$	1.644 ± 0.005 GeV	1.645 ± 0.005 GeV
e_1	1 (fixed)	1 (fixed)
e_2	0.052 ± 0.007	0.055 ± 0.007
e_3	0.295 ± 0.016	0.306 ± 0.016
G_1	0.044 ± 0.003 GeV	0.044 ± 0.003 GeV
G_2	0.217 ± 0.041 GeV	0.231 ± 0.041 GeV
G_3	0.295 ± 0.018 GeV	0.306 ± 0.018 GeV

than to the UFD result discussed here. Note also that the parametrization in [39] is a fit to data up to 1.8 GeV and that, in principle, it could be extrapolated up to 2.3 GeV.

E. D waves

1. $I = 3/2$ D wave

Once again, only Estabrooks *et al.* [22] provide data for the $I = 3/2$ D-wave phase shift up to 1.74 GeV, which we show in Fig. 8. Note it is very small in the whole energy region. No inelasticity has been measured so that we can use the elastic formalism parametrized with the conformal expansion in Eqs. (6) and (7), as follows:

$$\cot\delta_1^{3/2}(s) = \frac{\sqrt{s}}{2q^5}(B_0 + B_1\omega + B_2\omega^2). \tag{35}$$

Three conformal parameters are enough to describe this wave. As we did for the $P^{3/2}$ wave, the α parameter that defines the conformal variable ω in Eq. (7) has been chosen so that the center of the conformal expansion lies at the center of the region where data exists. Thus, for this wave we have set

$$\alpha = 1.45, \qquad s_0 = (1.84\ \text{GeV})^2. \tag{36}$$

As can be noticed in Fig. 8, there are sizable systematic uncertainties, which can be simply taken into account by multiplying the statistical uncertainties by $\sqrt{2}$. The resulting fit yields a $\chi^2/\text{d.o.f} \simeq 1.1$. However, as happened with the $S^{3/2}$ and $P^{3/2}$ waves, our final fit for the $I = 3/2$ D wave is obtained from a simultaneous fit to the data for this wave alone together with the data on the $t_D \equiv t_2^{1/2} + t_2^{3/2}/2$ combination obtained by Estabrooks *et al.* [22] and Aston *et al.* [24]. The parameters of such an UFD are given in Table VIII and we show the resulting phase shift as a continuous line in Fig. 8, where the gray band covers the corresponding uncertainty.

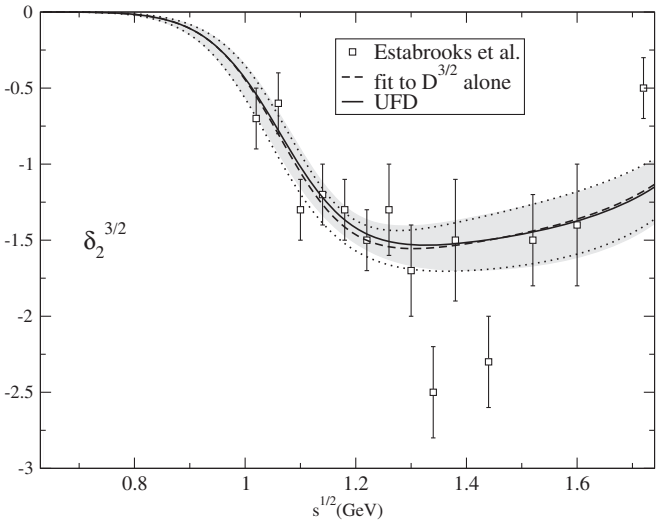

FIG. 8. Data on the $I = 3/2$ D wave from Estabrooks *et al.* [22]. We also show our UFD result as a solid line with a gray uncertainty band, which is obtained by fitting this data in a simultaneous fit with the data on the $t_2^{1/2} + t_2^{3/2}/2$ combination. For comparison we show with a dashed line a fit only to the data in this figure.

TABLE VIII. Parameters of the $D^{3/2}$ wave.

Parameter	UFD	CFD
B_0	-1.70 ± 0.12	-1.67 ± 0.12
B_1	-6.5 ± 1.7	-7.0 ± 1.7
B_2	-36 ± 9	-38 ± 9

In Fig. 8 we also show, as a dashed line, the result when fitting only the data in that figure and not the data on the t_D combination. The corresponding uncertainty band is delimited by dotted lines. As we can see it is very similar to our UFD curve.

2. $I = 1/2$ D wave

As happened with the S and P waves, the $I = 1/2$ D wave is only measured together with the $I = 3/2$ wave in the $t_D \equiv t_2^{1/2} + t_2^{3/2}/2$ combination. In the literature it is usual to neglect the $D^{3/2}$ wave, because as we have just seen it is very small, but we will keep it in our fits for completeness.

Let us then describe our fit to the $D^{1/2}$ wave, which is dominated by the $K_2^*(1430)$ resonance, whose branching ratio to πK is approximately 50%, so that we have to use an inelastic formalism as in Eqs. (8), (9), (10). In practice, it is enough to consider a nonresonant background and a resonantlike form, as follows:

$$t_2^{1/2} = \frac{S_0^b S_1^r - 1}{2i\sigma(s)}, \tag{37}$$

with a background term

$$S_0^b = e^{2i(p(s))}, \tag{38}$$

where

$$p(s) = \phi_0 q_{\eta K}^5 \Theta_{\eta K}(s) + q_{\eta' K}^5 \phi_1 \Theta_{\eta' K}(s),$$

and $\Theta_{ab} = \Theta(s - (m_a + m_b)^2)$. A resonant term is also considered in order to describe easily the $K_2^*(1430)$ shape, namely,

$$S_1^r = \frac{s_{r1} - s + i(P_1 - Q_1)}{s_{r1} - s - i(P_1 + Q_1)},$$
$$P_1 = e_1 G_1 \frac{p_1(q_{\pi K})}{p_1(q_{\pi K}^r)} \left(\frac{q_{\pi K}}{q_{\pi K,r}}\right)^5,$$
$$Q_1 = (1 - e_1) G_1 \frac{p_1(q_{\pi K})}{p_1(q_{\pi K}^r)} \left(\frac{q_{\eta K}}{q_{\eta K,r}}\right)^5 \Theta_{\eta K}(s), \quad (39)$$

with $p_1(q_{\pi K}) = 1 + a q_{\pi K}^2$.

3. t_D wave

Once more we define

$$t_D(s) \equiv |t_D(s)| e^{i\phi_D(s)}, \qquad \hat{t}_D(s) = t_D(s)\sigma(s). \quad (40)$$

Thus, in Figs. 9 and 10 we show the data on $|\hat{t}_D|$ and Φ_D, respectively. As we did for the P wave, we have treated the systematic uncertainties as follows: we have performed a first fit and added a systematic uncertainty to those isolated data points that are incompatible with it. This systematic uncertainty is half of their distance to the central value of the fit. In regions where the two sets of data are incompatible the systematic uncertainty is half of the average difference from the fit to each set in that region. With these additional systematic uncertainties we have performed a final fit, called an UFD, which is shown as a continuous line in Figs. 9 and 10. The UFD uncertainty is represented by a gray band. The total χ^2/d.o.f. is $49/(44-6+1)$. In addition, we show as a dashed line the result that is obtained if only the data on $\hat{t}_D$ from Aston *et al.* [24] is fitted. The central values are almost indistinguishable

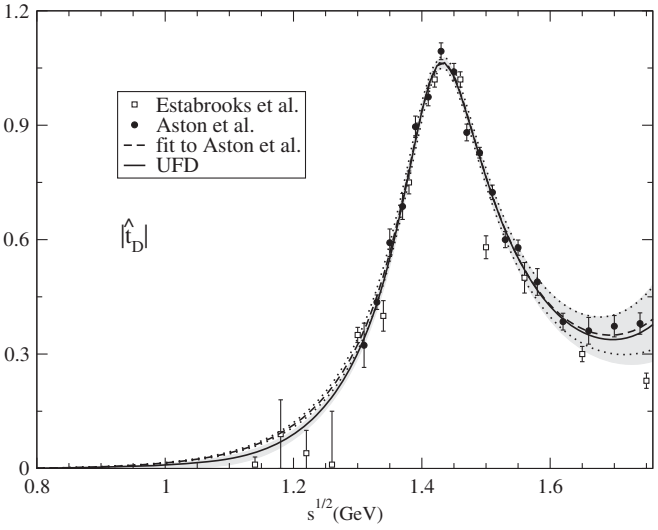

FIG. 9. Data on $|\hat{t}_D(s)|$ from [22,24]. The continuous line is our unconstrained fit (UFD), whose uncertainties are covered by the gray band. For comparison we show, as a dashed line, a fit only to the data from [24], whose corresponding uncertainties are delimited by the dotted lines.

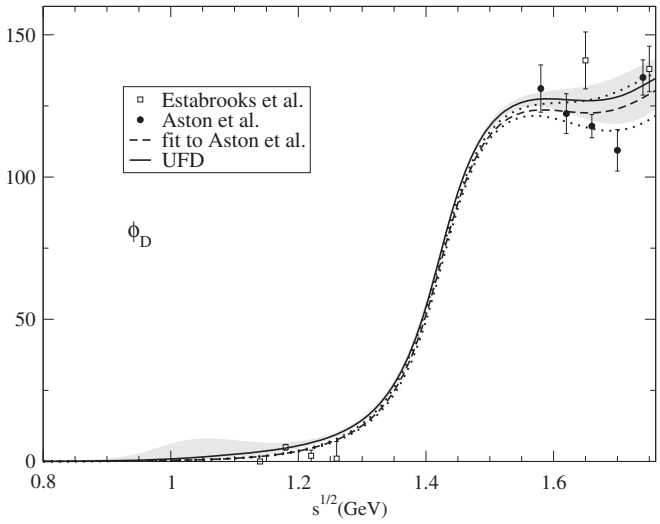

FIG. 10. Data on $\phi_D(s)$ from [22,24]. The continuous line is our unconstrained fit (UFD), whose uncertainties are covered by the gray band. For comparison we show, as a dashed line, a fit only to the data from [24], whose corresponding uncertainties are delimited by the dotted lines.

but the uncertainties are smaller. We still prefer our UFD parametrization because it contains more experimental information, although the uncertainties come larger due to the systematic uncertainties that we have taken into account in our UFD set. The UFD parameters are shown in Table IX.

F. $F^{1/2}$ wave

Once more we define

$$t_F(s) \equiv |t_F(s)| e^{i\phi_F(s)}, \qquad \hat{t}_F(s) = t_F(s)\sigma(s). \quad (41)$$

For this wave there are no observations of an $I = 3/2$ channel, which is neglected in the literature as will be done here too. In addition, the threshold suppression is so large that there are no data below 1.5 GeV, as can be seen in Figs. 11 and 12. In the latter we can observe that there are only two data points with very large uncertainties for the phase ϕ_F below 1.85 GeV. Thus, in order to stabilize our fit we will extend our data sample to 2 GeV, although later on

TABLE IX. Parameters of the $D^{1/2}$ fit.

Parameters	UFD	CFD
ϕ_0	2.17 ± 0.26 GeV^{-5}	3.00 ± 0.26 GeV^{-5}
ϕ_1	-12.1 ± 1.7 GeV^{-5}	-9.3 ± 1.7 GeV^{-5}
$\sqrt{s_{r1}}$	1.446 ± 0.002 GeV	1.445 ± 0.002 GeV
e_1	0.466 ± 0.006	0.465 ± 0.006
G_1	0.220 ± 0.009 GeV	0.222 ± 0.009 GeV
a	-0.53 ± 0.16 GeV^{-2}	-0.72 ± 0.16 GeV^{-2}

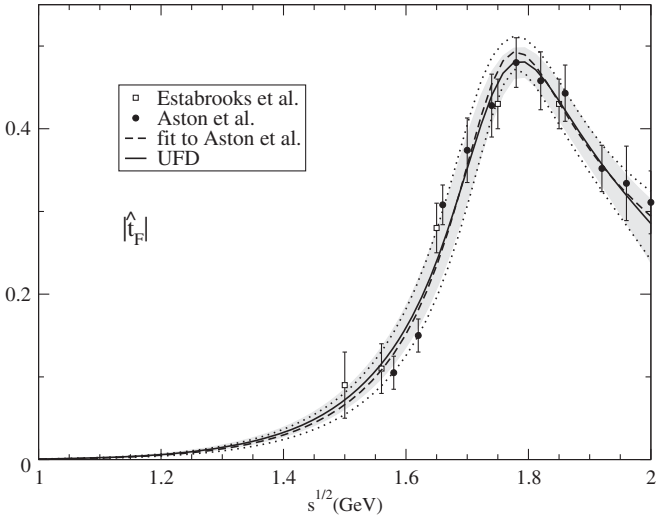

FIG. 11. Data on $|\hat{t}_F(s)|$ from [22,24]. The continuous line is our unconstrained fit (UFD), whose uncertainties are covered by the gray band. For comparison we show, as a dashed line, a fit to the data from [24], whose corresponding uncertainties are delimited by the dotted lines.

we will only make use of our partial wave parametrizations up to 1.74 GeV.

The most salient feature of this wave is the $K_3^*(1780)$ resonance, whose branching ratio to πK is slightly less than 20%. Therefore we will need the usual inelastic formalism explained in the Introduction to this section:

$$t_3^{1/2} = \frac{S_1^r - 1}{2i\sigma(s)}, \tag{42}$$

with

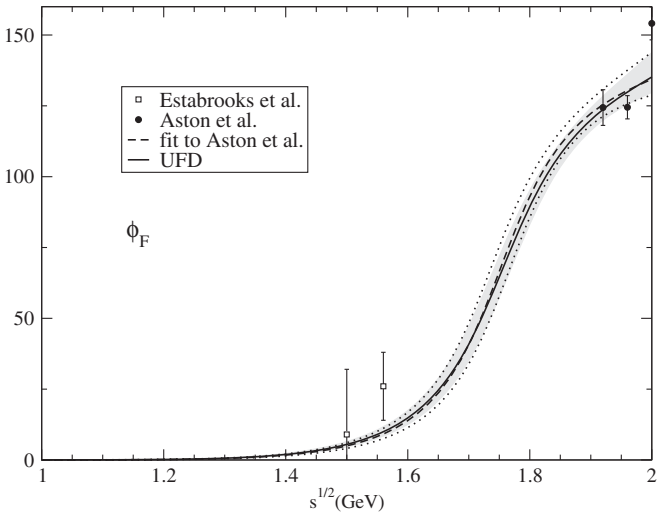

FIG. 12. Data on $\phi_F(s)$ from [22,24]. The continuous line is our unconstrained fit (UFD), whose uncertainties are covered by the gray band. For comparison we show, as a dashed line, a fit to the data from [24], whose corresponding uncertainties are delimited by the dotted lines.

TABLE X. Parameters of the $F^{1/2}$ wave.

Parameters	UFD	CFD
$\sqrt{s_{r1}}$	1.801 ± 0.013 GeV	1.804 ± 0.013 GeV
e_1	0.181 ± 0.006	0.184 ± 0.006
G_1	0.47 ± 0.05 GeV	0.50 ± 0.05 GeV
a	-0.88 ± 0.10 GeV^{-2}	-0.97 ± 0.10 GeV^{-2}

$$S_1^r = \frac{s_{r1} - s + i(P_1 - Q_1)}{s_{r1} - s - i(P_1 + Q_1)},$$
$$P_1 = e_1 G_1 \frac{p_1(q_{\pi K})}{p_1(q_{\pi K}^r)} \left(\frac{q_{\pi k}}{q_{\pi k,r}}\right)^7,$$
$$Q_1 = (1 - e_1) G_1 \frac{p_1(q_{\pi K})}{p_1(q_{\pi K}^r)} \left(\frac{q_{\eta k}}{q_{\eta k,r}}\right)^7 \Theta_{\eta K}(s). \tag{43}$$

In addition, $p_1(q_{\pi K}) = 1 + a q_{\pi K}^2$ and $\Theta_{\eta K}(s) = \Theta(s - (m_\eta + m_K)^2)$.

No background term is needed for this wave because its behavior is well described using the resonantlike form only, as can be observed in Figs. 11 and 12. The fit yields $\chi^2/\text{d.o.f.} = 16/(21 - 4 + 1)$ and the UFD parameters listed in Table X.

G. Regge parametrization

There are no data on $I = 3/2$ above 1.74 GeV, thus above that energy we will make use of the Regge parametrization for πK scattering in [17,40], which was obtained from factorization after fitting data on NN, $N\pi$, NK and $\pi\pi$ high energy scattering. Note that for πK scattering only the exchange of isospin 0 and 1 can occur in the t channel.

For the isoscalar exchange there are two contributions: the Pomeron, called $P(s)$ here, and the subleading f_2 trajectory, called $P'(s)$, so that we write

$$\text{Im}T_{\pi K}^{(I_t=0)}(s,t) = f_{K/\pi}[P(s,t) + rP'(s,t)], \tag{44}$$

where

$$P(s,t) = \beta_P \psi_P(t) \alpha_P(t) \frac{1 + \alpha_P(t)}{2} e^{bt} \left(\frac{s}{s'}\right)^{\alpha_P(t)},$$
$$P'(s,t) = \beta_{P'} \psi_{P'}(t) \frac{\alpha_{P'}(t)(1 + \alpha_P(t))}{\alpha_{P'}(0)(1 + \alpha_P(0))} e^{bt} \left(\frac{s}{s'}\right)^{\alpha_{P'}(t)},$$
$$\alpha_P(t) = 1 + t\alpha_P', \qquad \psi_P = 1 + c_P t,$$
$$\alpha_{P'}(t) = \alpha_{P'}(0) + t\alpha_{P'}', \qquad \psi_P = 1 + c_{P'} t. \tag{45}$$

Note that, by using factorization, the substitution of the $\pi\pi$-Pomeron vertex by the KK-Pomeron vertex is taken into account by the $f_{K/\pi}$ constant, whereas $rf_{K/\pi}$ takes care of the similar factorization for P'.

Since in this work we are interested in forward dispersion relations, we will only use the above Regge formulas with $t = 0$, but we provide the full expressions for completeness.

For the isovector exchange only the ρ trajectory is needed and we use

$$\mathrm{Im}T_{\pi K}^{(I_t=1)}(s,t) = g_{K/\pi}\mathrm{Im}T_{\pi\pi}^{(I_t=1)}(s,t), \tag{46}$$

with

$$\mathrm{Im}T_{\pi\pi}^{(I_t=1)}(s,t) = \beta_\rho \frac{1+\alpha_\rho(t)}{1+\alpha_\rho(0)}\varphi(t)e^{bt}\left(\frac{s}{s'}\right)^{\alpha_\rho(t)},$$
$$\alpha_\rho(t) = \alpha_\rho(0) + t\alpha'_\rho + \frac{1}{2}t^2\alpha''_\rho,$$
$$\varphi(t) = 1 + d_\rho t + e_\rho t^2. \tag{47}$$

Once again, the replacement of the $\pi\pi\rho$ vertex by the $KK\rho$ one is described by the $g_{K/\pi}$ constant, assuming factorization. Note that in [17] the value of $g_{K/\pi} = 1.1 \pm 0.1$ was used together with $\beta_\rho = 0.94 \pm 0.20$ to provide a description of πK. However, the same group [40] updated their $\pi\pi$ scattering analysis using dispersion relations and $\pi\pi$ scattering data at high energies to find $\beta_\rho = 1.48 \pm 0.14$. Consequently, if we want to use this latter value, we also have to update $g_{K/\pi} = 0.70 \pm 0.07$. One should nevertheless take into account that the information on this parameter is relatively scarce, since, in contrast to $\pi\pi$ scattering, there are no high energy data on πK scattering.

TABLE XI. Values of Regge parameters obtained in [17,40]. Since these could be fixed using reactions other than πK scattering, they will be fixed in both our UFD and CFD parametrizations.

Regge parameters	Used for both UFD and CFD
s'	1 GeV^2
b	2.4 ± 0.5 GeV^{-2}
α'_ρ	0.9 GeV^{-2}
α''_ρ	-0.3 GeV^{-4}
d_ρ	2.4 ± 0.5 GeV^{-2}
e_ρ	2.7 ± 2.5
α'_P	0.2 ± 0.1 GeV^{-2}
$\alpha'_{P'}$	0.9 GeV^{-2}
c_P	0.6 ± 1 GeV^{-2}
$c_{P'}$	-0.38 ± 0.4 GeV^{-2}
β_ρ	1.48 ± 0.14
$\alpha_\rho(0)$	0.53 ± 0.02
β_P	2.50 ± 0.04
$c_P(0)$	0 ± 0.04
$\beta_{P'}$	0.80 ± 0.05
$c_{P'}(0)$	-0.4 ± 0.4
β_2	0.08 ± 0.2
$\alpha_{P'}(0)$	0.53 ± 0.02

TABLE XII. Values of Regge parameters directly related to πK scattering. In practice r does not change from the UFD to the CFD parametrization.

Parameters	UFD	CFD
$f_{K/\pi}$	0.67 ± 0.01	0.66 ± 0.01
r	5×10^{-2}	5×10^{-2}
$g_{K/\pi}$	0.70 ± 0.07	0.53 ± 0.07

Thus it has to be determined only from factorization of KN scattering. Note that β_ρ, which is the equivalent value for $\pi\pi$, suffered a large revision when taking into account dispersion relations. Thus, large deviations in $g_{K/\pi}$ should not come as a surprise and they actually do occur when imposing our dispersive constraints on πK scattering.

The set of Regge parameters used before imposing any πK dispersion relation will be labeled as UFD values, similar to what we have been doing so far with our partial wave parametrizations. Correspondingly, we will refer to CFD values when in the next sections forward dispersion relations will be imposed on our fits. Those Regge parameters that could be determined without $K\pi$ input are shown in Table XI and their values are fixed both for the UFD and CFD parametrizations. They just correspond to the values in the original works [17,40].

In contrast, the values $f_{K/\pi}$, $g_{K/\pi}$ and r, which are directly related to πK scattering, are listed in Table XII and in this work they are allowed to vary from the UFD to the CFD parametrization, although in practice r stays the same.

IV. FORWARD DISPERSION RELATIONS AND SUM RULES

The aim of this work is to provide a simple set of partial waves which are consistent with basic requirements of analyticity (or causality) and crossing. These features impose stringent constraints on the scattering amplitude, which translate into integral equations that relate the πK scattering amplitude at a given energy with an integral over the whole physical energy region. In this section we introduce a complete set of forward dispersion relations that will be used first to check the consistency of our parametrizations and next as constraints on our fits.

A. Forward dispersion relations

Forward dispersion relations (FDRs), i.e., those calculated at $t = 0$, are useful because forward scattering is relatively easy to measure in the whole energy region, since it is related to the total cross section by the optical theorem. Moreover, this is the only fixed value of t for which the integrands in the dispersion relation will be given directly in terms of the imaginary part of a physical amplitude. They are applicable at any energy, in contrast to Roy-like equations, which, in practice, have a limited applicability energy range due to the projection in partial waves.

Fixed-t dispersion relations for πK have been frequently used in the literature as an intermediate step for the derivation of more elaborate dispersion relations for partial waves [14,15,41–43], or of sum rules for low-energy parameters [4], but not directly as constraints on the amplitudes, as will be done here.

For the sake of simplicity, given that $s+t+u=2(m_K^2+m_\pi^2)$ and $t=0$, it is customary to use an abbreviated notation $T(s,t=0,u)=T(s)$. It is also very convenient to make use of $s\leftrightarrow u$ crossing to change the amplitudes from the isospin basis to the $s\leftrightarrow u$ symmetric and antisymmetric amplitudes. These are defined, respectively, as

$$T^+(s)=\frac{T^{1/2}(s)+2T^{3/2}(s)}{3}=\frac{T^{I_t=0}(s)}{\sqrt{6}},$$
$$T^-(s)=\frac{T^{1/2}(s)-T^{3/2}(s)}{3}=\frac{T^{I_t=1}(s)}{2}. \tag{48}$$

In the last step we have indicated that T^+ and T^- correspond, by crossing, to the exchange of isospin 0 or 1 in the t channel, respectively. This is relevant because it means that T^+ is dominated at high energies by the t-channel exchanges of the Pomeron and P' trajectories, with no ρ trajectory contribution, whereas the opposite occurs for T^-.

Since dispersive integrals extend to infinity, naively one would need two subtractions to ensure the convergence of the Pomeron contribution and one for that of the ρ trajectory. For this reason, even if only used as intermediate steps for the derivation of other dispersion relations, the fixed-t dispersion relations for T^+ are customarily written with two subtractions and those for T^- with at least one. However, this is not necessary, because the $T^\pm$ FDRs have integrals over the right-hand and left-hand cuts whose leading terms multiplying the Regge trajectories cancel against each other due to the symmetry properties. As a consequence, one subtraction is enough to ensure the convergence of the T^+ FDR and no subtraction is needed for the T^- FDR. These kinds of cancellations have been recently used for $\pi\pi$ scattering FDRs in [17,40,44,45]. Having more subtractions implies that the dispersion relation is determined up to a polynomial of higher order. Thus, generically, fewer subtractions are convenient to avoid the propagation of the uncertainties in the subtraction constants to become too large in the resonance region, whereas more subtractions are useful when concentrating on the threshold region. Since in this work we will deal with scattering up to 1.74 GeV, we will make use of FDRs with the minimum number of subtractions needed, which also makes the equations slightly simpler.

Thus, for T^+ the once-subtracted FDR reads

$$\mathrm{Re}T^+(s)=T^+(s_{\rm th})+\frac{(s-s_{\rm th})}{\pi}P\int_{s_{\rm th}}^{\infty}ds'\left[\frac{\mathrm{Im}T^+(s')}{(s'-s)(s'-s_{\rm th})}-\frac{\mathrm{Im}T^+(s')}{(s'+s-2\Sigma_{\pi K})(s'+s_{\rm th}-2\Sigma_{\pi K})}\right], \tag{49}$$

where $s_{\rm th}=(m_\pi+m_K)^2$ and P stands for the principal part of the integral. In contrast, the unsubtracted FDR for T^- reads

$$\mathrm{Re}T^-(s)=\frac{(2s-2\Sigma_{\pi K})}{\pi}P\int_{s_{\rm th}}^{\infty}ds'\frac{\mathrm{Im}T^-(s')}{(s'-s)(s'+s-2\Sigma_{\pi K})}. \tag{50}$$

We have evaluated these two FDRs at 50 values of $\sqrt{s_i}$ equally spaced between a minimum energy $\sqrt{s_{\rm min}}$ and 1.74 GeV, using as input for the integrals our UFD partial waves at $s'\leq 1.74$ GeV and the Regge UFD parametrizations above. At each of these $\sqrt{s_i}$'s we have also calculated the difference d_i between the left- and right-hand sides of each FDR as well as its corresponding uncertainty Δd_i. When $d_i\lesssim\Delta d_i$ we can consider that the FDR is satisfied within uncertainties at the energy $\sqrt{s_i}$.

As a word of caution, let us remark that the uncertainties Δd_i are calculated as the quadratic addition of the uncertainties due to the error bar of each parameter in the UFD parametrization. Note however that in the full physical amplitude, being a solution of the FDRs, all these parameters would be correlated. Our parametrizations are just a fit to partial waves, many of which have been measured independently from one another, and these correlations may be lost. Therefore our FDR error bands only reflect the propagation of the uncertainties from our data parametrizations, without the possible correlations between parameters that may exist.

The results of the above calculation for T^+ are shown in the upper panel of Fig. 13. We plot $\mathrm{Re}T^+$ calculated directly from the UFD parametrization (input UFD) versus $\mathrm{Re}T^+$ calculated from the dispersive representation in Eq. (49) above (dispersive UFD). The gray area corresponds to adding $\pm\Delta d_i$ to the "dispersive UFD" curve. Note that for this symmetric amplitude we have set $\sqrt{s_{\rm min}}$ at $K\pi$ threshold. We can see that the input UFD lies slightly beyond the uncertainty band up to 1.2 GeV, but that it is much more separated beyond 1.55 GeV. The consistency of the data with the T^+ FDR is therefore not very satisfactory, particularly at higher energies.

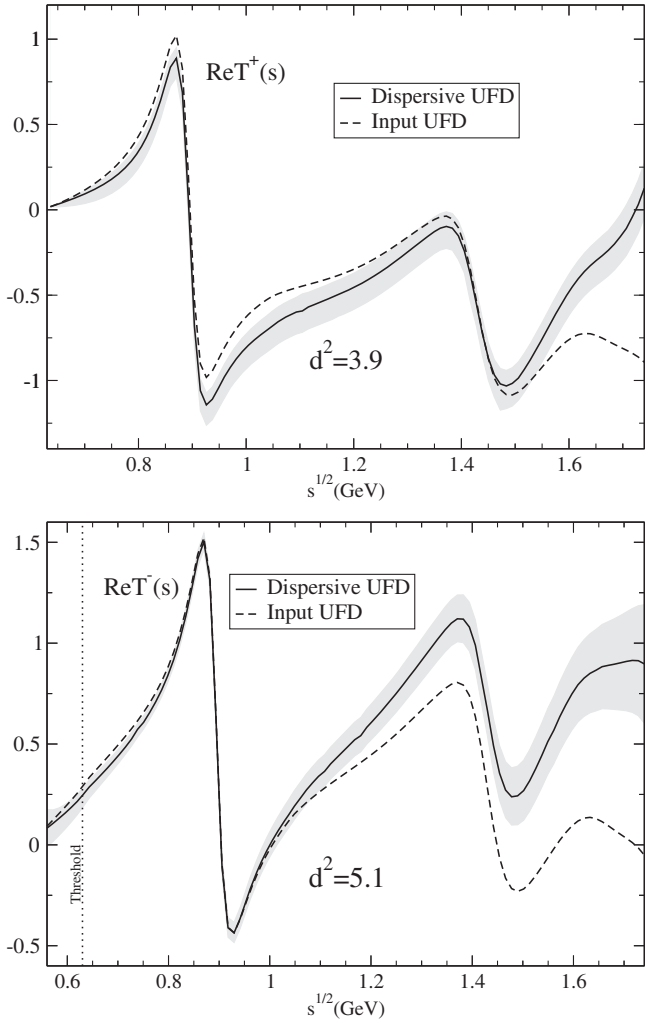

FIG. 13. Comparison between the input (dashed lines) and the output for the T^+ (top panel) and T^- (bottom panel) FDRs when using the UFD set. These correspond to the left-hand side versus the right-hand side in Eqs. (49) and (50). The gray bands describe the uncertainty of the difference.

The results for T^- are plotted in the lower panel of Fig. 13, using the same conventions. In this case we have set $\sqrt{s_{\rm min}} = 0.56$ GeV, below threshold, because the T^- FDR has no subtractions and thus provides strong constraints on a combination of scalar scattering lengths. The figure shows that the separation between both calculations is slightly above Δd_i up to 0.8 GeV. Above this energy, the T^- FDR is nicely satisfied within uncertainties up to 1.2 GeV, where the difference between the two curves starts growing, becoming much larger than Δd_i. As we will see, the deviation at energies above 1.2 GeV is mainly caused by the ρ-exchange Regge contribution.

In order to provide a quantitative measure of the fulfillment of each FDR, we have defined an averaged squared distance for each FDR,

TABLE XIII. Fulfillment of forward dispersion relations (FDRs) in different energy regions. We provide the averaged square distance divided by relative error between the left- and right-hand sides of each FDR. Note the remarkable improvement from the UFD to the CFD parametrization.

	UFD		CFD	
	$d^2_{T^+}$	$d^2_{T^-}$	$d^2_{T^+}$	$d^2_{T^-}$
$\sqrt{s_{\rm min}} \le \sqrt{s} \le m_K + m_\eta$	3.35	0.97	0.39	0.13
$m_K + m_\eta \le \sqrt{s} \le 1.6$ GeV	1.3	6.8	0.17	0.70
1.6 GeV $\le \sqrt{s} \le 1.74$ GeV	14.6	12.8	8.0	0.5
$\sqrt{s_{\rm min}} \le \sqrt{s} \le 1.74$ GeV	3.9	5.1	1.3	0.44

$$d^2_{T\pm} = \frac{1}{N}\sum_{i=1}^{N}\left(\frac{d_i}{\Delta d_i}\right)^2_{T^\pm}, \tag{51}$$

which is rather similar to the usual definition of a χ^2 function. Consistency of the data parametrizations with FDRs would demand $d^2_{T\pm} \lesssim 1$.

In Table XIII we show the values of $d^2_{T\pm}$ in different energy regions. For the UFD set it is clear that the consistency with FDRs is not very satisfactory, particularly in the inelastic region, and very inconsistent above 1.6 GeV. There is room for the considerable improvement that will be achieved in Sec. V, to the point of obtaining a constrained set of parametrizations (CFD) remarkably consistent with both FDRs up to 1.6. However, we will see that above that energy we are only able to improve the agreement but not achieve consistency within uncertainties.

B. Sum rules for threshold parameters

Threshold parameters of partial waves, defined in Eq. (5), are of interest for our understanding of the lowest energy physics and particularly for studies within ChPT [1]. In this section we present three sum rules (SRs) that provide a more accurate determination of certain combinations of threshold parameters, in terms of integrals, than would be achieved directly from the partial wave parametrizations. These SRs will be used first as tests of our UFD parametrizations and in Sec. V will be used as constraints.

Other sum rules have been derived for determining the ChPT low-energy constants [4], but here we will use our own sum rules for threshold parameters. In [14] a sum rule for a combination of scattering lengths is given, but it needs $\pi\pi \to K\bar{K}$ scattering input, and here we only want to use data on πK scattering.

Thus, the first of our sum rules yields precisely the combination of scalar scattering lengths measured at DIRAC [38], see Eq. (24) above. It is basically the T^- FDR evaluated at threshold and for convenience we will write it as follows:

TABLE XIV. Sum rules in m_π units. We show results for the UFD and CFD parametrizations. Note that since $a_1^{3/2}$ is more than 30 times smaller than $b_0^{3/2}$, then $D_{3/2} \sim b_0^{3/2}$.

	UFD	CFD
D_a	$0.108^{+0.018}_{-0.010}$	$0.091^{+0.006}_{-0.005}$
SR_a	0.093 ± 0.004	0.091 ± 0.003
Δ_a	$0.015^{+0.020}_{-0.012}$	$0.000^{+0.006}_{-0.005}$
$D_{1/2}$	$0.205^{+0.039}_{-0.024}$	$0.187^{+0.023}_{-0.016}$
$SR_{1/2}$	$0.186^{+0.006}_{-0.006}$	$0.182^{+0.006}_{-0.005}$
$\Delta_{1/2}$	$0.019^{+0.038}_{-0.024}$	$0.005^{+0.022}_{-0.016}$
$D_{3/2}$	$-0.051^{+0.037}_{-0.005}$	$-0.047^{+0.005}_{-0.005}$
$SR_{3/2}$	$-0.046^{+0.003}_{-0.011}$	$-0.041^{+0.002}_{-0.002}$
$\Delta_{3/2}$	$-0.005^{+0.048}_{-0.007}$	$-0.006^{+0.006}_{-0.006}$

$$0 = \Delta_a \equiv D_a - SR_a, \tag{52}$$

where

$$D_a \equiv \frac{1}{3}(a_0^{1/2} - a_0^{3/2}) \tag{53}$$

is calculated "directly" from our parametrizations. In principle it should be equal to the following integral expression:

$$SR_a \equiv \frac{2m_\pi m_K}{\sqrt{s_{th}}} P \int_{s_{th}}^{\infty} \frac{\mathrm{Im}T^-(s')}{s'(s'-s_{th})} ds'.$$

In practice, since D_a and SR_a are obtained from data the sum rule will not be exactly zero, but consistency requires it to cancel within uncertainties.

In Table XIV we show the results of this sum rule calculation using our UFD parametrizations. Note that it is not very well satisfied, since the Δ_a is slightly above 1.2 deviations from zero. This small disagreement suggests that there is room for improvement at low energies in the S waves. Both the direct and integral results are compatible with the experimental value obtained in DIRAC, Eq. (24), but this is not surprising given the very large experimental uncertainties.

Let us remark that a sum rule involving only scalar scattering lengths cannot be derived from the T^+ FDR because it has one subtraction. However, from once-subtracted FDRs it is possible to obtain sum rules involving scalar slope parameters and vector scattering lengths. Actually, by combining the T^+ FDR in Eq. (49) and the once-subtracted version of the T^- FDR, we can obtain two independent sum rules. Once again we will write them as

$$0 = \Delta_I \equiv D_I - SR_I, \tag{54}$$

with $I = 1/2, 3/2$. On the one hand,

$$D_I \equiv b_0^I + 3a_1^I \tag{55}$$

will be calculated directly from the parametrizations. Note that $a_1^{3/2}$ is more than 30 times smaller than $b_0^{3/2}$, so that $D_{3/2} \sim b_0^{3/2}$ is a very good approximation. On the other hand, the SR_I's are calculated with the following integral expressions:

$$SR_{1/2} \equiv \frac{\sqrt{s_{\mathrm{th}}}}{2m_\pi m_K} \times P \int_{s_{\mathrm{th}}}^{\infty} ds' \left[\frac{\mathrm{Im}T^+(s') + 2\mathrm{Im}T^-(s')}{(s'-s_{\mathrm{th}})^2} - \frac{\mathrm{Im}T^+(s') - 2\mathrm{Im}T^-(s')}{(s'+s_{\mathrm{th}}-2\Sigma_{\pi K})^2} \right], \tag{56}$$

and

$$SR_{3/2} \equiv \frac{\sqrt{s_{\mathrm{th}}}}{2m_\pi m_K} \times P \int_{s_{\mathrm{th}}}^{\infty} ds' \left[\frac{\mathrm{Im}T^+(s') - \mathrm{Im}T^-(s')}{(s'-s_{\mathrm{th}})^2} - \frac{\mathrm{Im}T^+(s') + \mathrm{Im}T^-(s')}{(s'+s_{\mathrm{th}}-2\Sigma_{\pi K})^2} \right]. \tag{57}$$

In Table XIV we show the results of these sum rules when the UFD set is used as input. As expected, the integral result, SR_I, is more accurate than the direct evaluation, D_I, for both sum rules. Although the fulfillment of these sum rules by our UFD set is fairly good, this is mostly due to the large and very asymmetric uncertainties in D_I, to not very good agreement in the central values.

In summary, the UFD set leaves room for improving the fulfillment of the sum rules just discussed. Hence in Sec. V they will be considered, together with the FDRs, as constraints for our parametrizations.

V. CONSTRAINED FITS TO DATA

So far we have used the FDRs and sum rules as checks of our UFD set. We have seen that there is room for improvement and therefore in this section we will use them as constraints to obtain a new set of parametrizations, that we will call the CFD set. In particular we will minimize the following quantity:

$$W^2(d_{T^+}^2 + d_{T^-}^2) + \sum_{I=\frac{1}{2},\frac{3}{2}} \left(\frac{\Delta_I}{\delta\Delta_I} \right)^2 + \sum_k \left(\frac{p_k^{UFD} - p_k}{\delta p_k^{UFD}} \right)^2, \tag{58}$$

where $d_{T^\pm}^2$ are the average square distances between the FDR input and output defined in Eq. (51), Δ_I are the sum rules defined in Eq. (54) and $\delta\Delta_I$ are their associated

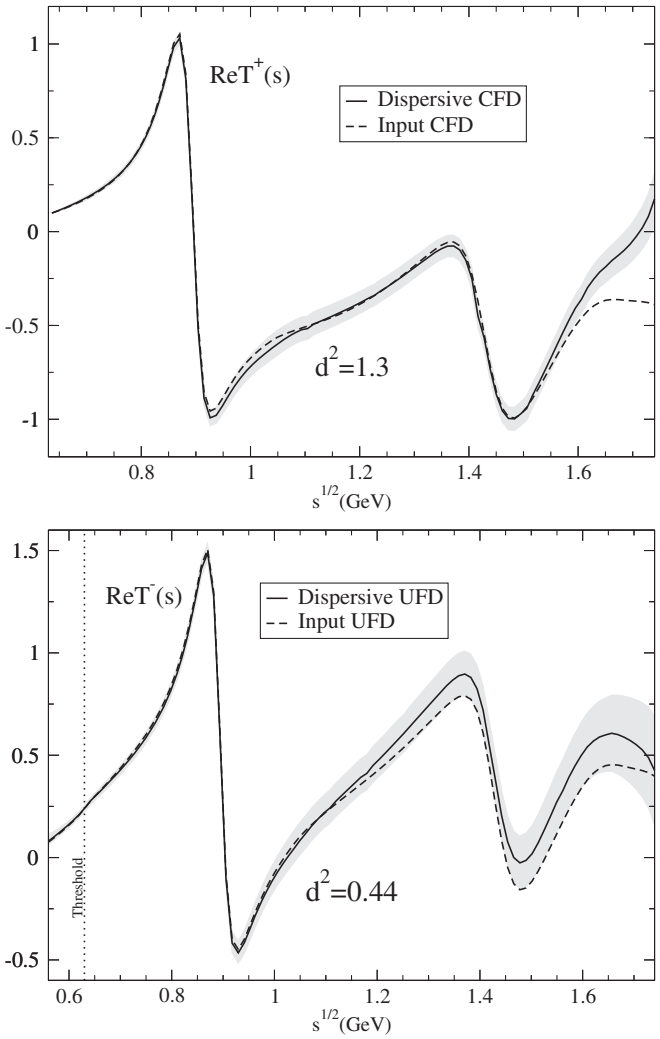

FIG. 14. Comparison between the input (dashed line) and the output for the T^+ (top panel) and T^- (bottom panel) FDRs when using the CFD set. These correspond to the left-hand side versus the right-hand side, respectively, in Eqs. (49) and (50). The gray bands describe the uncertainty of the difference. Note the dramatic improvement below 1.6 GeV compared to the results in Fig. 13 using the UFD set. Actually, the input and dispersive CFD calculations are consistent within uncertainties up to 1.6 GeV.

uncertainties. Note that the Δ_a sum rule of Eq. (52) is included in the $d^2_{T^-}$ term. Finally, to avoid large deviations from the UFD data description, we add a χ^2-like penalty function for each UFD parameter. Generically we have denoted these UFD parameters by p_k^{UFD} and their uncertainty by δp_k^{UFD}. The $W^2 = 12$ constant stands for the number of degrees of freedom observed naively from the shape of $\mathrm{Re}T^{\pm}$, which as seen in Fig. 14 is roughly 12. This approach is the same already followed for $\pi\pi$ scattering in [17,40,44,45].

With this minimization procedure we have arrived to a CFD set, whose parameters can be found in Tables I–III and V–X. Most CFD parameters are consistent within one deviation with their UFD counterparts. Actually, we have allowed 46 parameters to vary, of which 38 lie within 1 deviation, and only three lie beyond 1.6 deviations. These are the Φ_0 parameter of the $D^{1/2}$ wave, which changes by 3 deviations, the Regge $g_{K/\pi}$ parameters, changing by 2.5 deviations, and the B_2 parameter of the $S^{3/2}$ wave that changes by 1.8 deviations.

Before discussing in detail the changes from the UFD to the CFD set, let us discuss first how well this new CFD set satisfies the FDRs and sum rules.

A. FDRs and sum rules for the CFD set

In Fig. 14 we show the FDR results for the T^+ and T^- amplitudes using the CFD set as input. These have to be compared with the corresponding results for the UFD set in Fig. 13. Note that, in contrast to what happened when using the UFD set as input, the CFD input and its dispersive output now agree within uncertainties. The only exception is still the T^+ FDR above 1.6 GeV, where the agreement has nevertheless improved compared to the UFD result. For this reason in this work we only claim to have precise and consistent parametrizations up to 1.6 GeV. It seems that improving the agreement above this region would require our parametrizations to depart from data. This could be due to the existence of some large systematic uncertainties in some waves or to the fact that the whole tower of higher partial waves may start to play a more relevant role.

The results for the averaged distances $d^2_{T^\pm}$ of the two FDRs for this CFD set are shown in Table XIII. Let us remark that they are much smaller than 1 below 1.6 GeV. The CFD set is therefore remarkably consistent up to that energy, which is a dramatic improvement over the UFD set. In addition, from 1.6 to 1.74 GeV the antisymmetric FDR is also well satisfied. However, although the CFD improves on the fulfillment of the symmetric FDR above 1.6 GeV, it is still quite inconsistent. It has not been possible to fulfill the T^+ FDR above 1.6 GeV with an acceptable data description.

In Table XIV we have also provided the CFD result for the sum rules. The central value of all Δ_I's are now closer to zero and the uncertainties are much smaller and much more symmetric.

Thus, once we have seen that the consistency of the description has improved, let us study in detail the changes in the partial waves from the UFD to the CFD set, and check to see that they still provide a good description of data up to 1.6 GeV.

B. S waves

1. $S^{3/2}$ wave

The $S^{3/2}$-wave CFD parameters can be found in Table I. In Fig. 15 we show as a continuous line the CFD phase shift whose uncertainties are covered by the gray band,

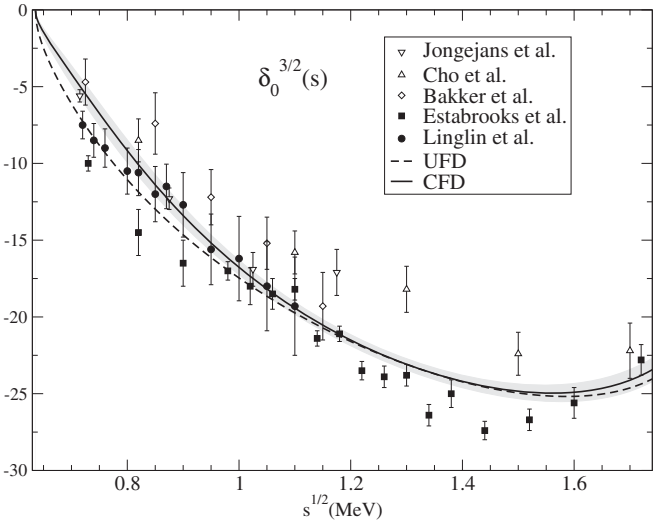

FIG. 15. The CFD parametrization of the $S^{3/2}$ wave is shown as a continuous line and its uncertainty as a gray band. For comparison the UFD parametrization is shown as a dashed line. See Fig. 1 for data references.

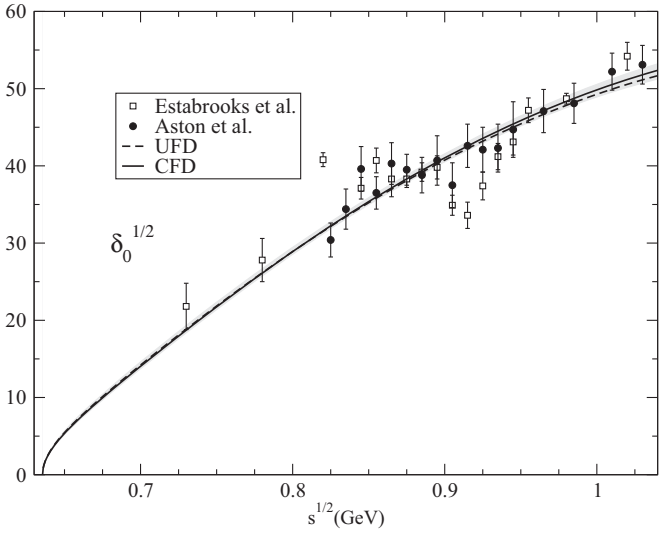

FIG. 16. CFD parametrization of the $S^{1/2}$-wave phase shift in the elastic region, shown as a continuous line whose uncertainty is covered by the gray band. For comparison we also show as a dashed line the UFD result. Note that in this case the UFD and CFD parametrizations are almost indistinguishable. See Fig. 3 for data references.

whereas the UFD phase is represented by a dashed line. We do not plot the uncertainty band of the UFD curve because it was already given in Fig. 1 and it overlaps with the CFD band. From 1 to 1.74 GeV, the UFD and CFD fits are almost identical, although they differ at lower energies. In particular the central value of the CFD scattering length is about half of that obtained for the UFD, as seen in Table IV.

That some changes were needed at low energies in the scalar waves was to be expected since we already saw that the Δ_a sum rule was not satisfied very well by the UFD set. Moreover, in Fig. 13 a deviation in the low-energy region of the FDRs was also observed for the UFD set.

It turns out that the FDRs and sum rule constraints tend to correct these small deviations by modifying only the $S^{3/2}$ wave at low energies. Actually, note that both the B_1 and B_2 parameters of the $S^{3/2}$ wave change from their UFD values by 1.5 and 1.8 deviations, respectively. In contrast, imposing the FDR and sum rule constraints barely changes the $S^{1/2}$ wave in the elastic region, as we will see next. Note also that the CFD result strongly disfavors the Estabrooks *et al.* data at low energies. This may serve as *a posteriori* justification for those works that neglect these data from the start.

2. $S^{1/2}$ wave

As can be seen in Fig. 16 the CFD $S^{1/2}$ wave in the elastic region (the continuous line) is almost indistinguishable from the UFD parametrization. Actually, as seen in Table II, the B_0 parameter does not change at all, whereas the CFD B_1 central value lies within less than one deviation of the UFD parameter.

3. t_S wave

As explained in previous sections, the data in the inelastic region are presented in terms of the modulus and phase of the $\hat{t}_S$ amplitude. As seen now in Fig. 17, in the inelastic region the UFD and CFD descriptions are quite compatible up to 1.5 GeV. However, above that energy the CFD parametrization starts deviating from the UFD result. The UFD central value (the dashed line) lies slightly outside the uncertainty band of the CFD set, although both uncertainty bands would always overlap and therefore the CFD still provides a fairly good description of the data. Actually, it can be checked in Table III that the parameter of the CFD inelastic fit that varies the most with respect to its UFD value is ϕ_1, which changes by merely 1.1 deviations. Around 1.7 GeV the CFD result prefers the solution of Aston *et al.* [24] for the phase. This deviation of the CFD set from the UFD one reflects the fact that forward dispersion relations are not well satisfied by the UFD set in this region, as we already saw in Fig. 13. As a matter of fact, the S waves and the $D^{1/2}$ wave are the ones that change most to improve the consistency of the FDRs above 1.5 GeV.

C. P waves

1. $P^{3/2}$ wave

The CFD solution for this wave is shown as a continuous line in Fig. 18, where its uncertainty is covered by the gray band. Note that the UFD solution is compatible in the whole energy region with the new CFD parametrization. Moreover, in Table V it can be seen that the two CFD B_k

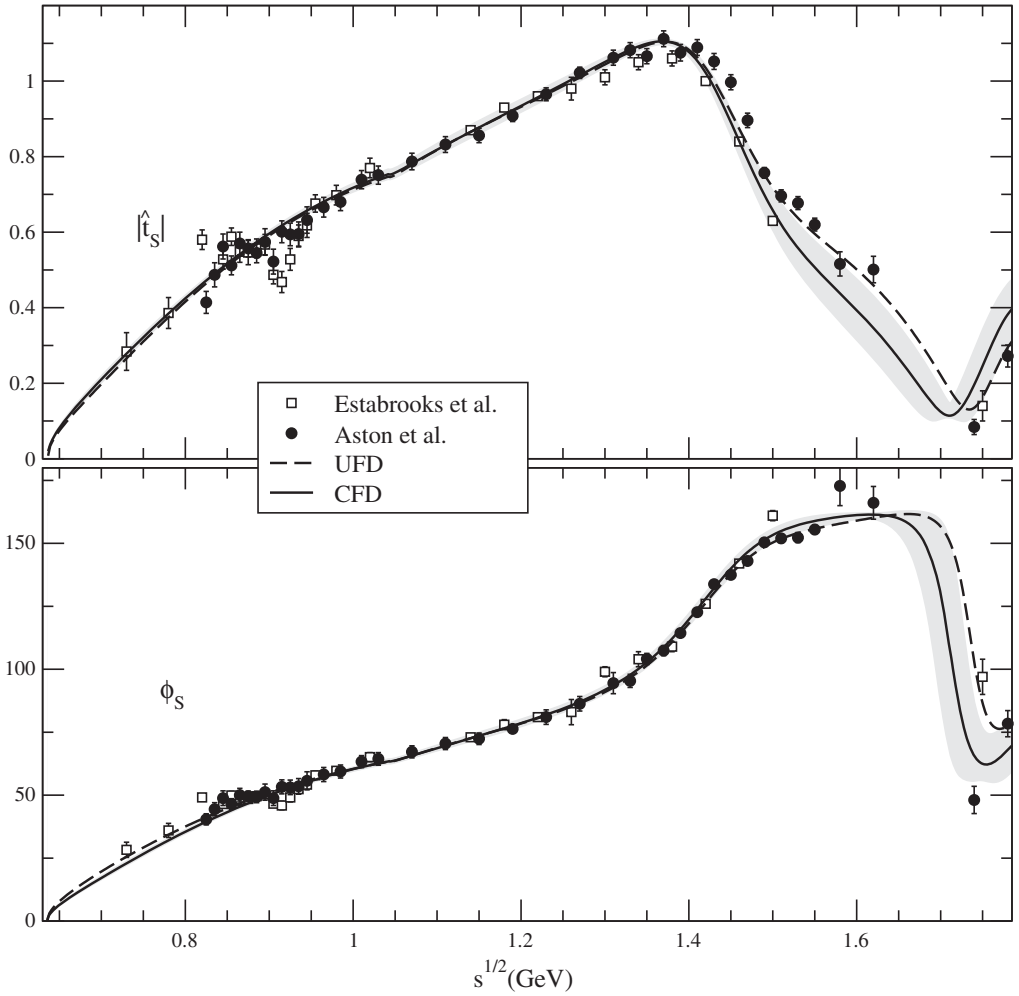

FIG. 17. CFD parametrization of the $\hat{t}_S$ wave in the whole energy region. On the upper panel we show $|\hat{t}_S(s)|$, whereas in the lower one we show $\phi_S(s)$. The continuous line is our constrained fit (CFD), whose uncertainties are covered by the gray band. For comparison we show the UFD result as a dashed line. Data references are as in Fig. 2.

parameters lie well within the uncertainties of their UFD counterparts. Therefore the data description is still acceptable.

Let us recall that although the absolute value of this phase shift is smaller than 2.5° in the whole energy region, this wave still has a sizable effect on our calculations. This is partly due to the $(2l+1)$ factors in Eq. (1), but particularly because all other waves become relatively small around 1.5 GeV.

2. $P^{1/2}$ wave

As seen in Fig. 19 the CFD (continuous line) and UFD (dashed) fits are almost indistinguishable up to 930 MeV despite the very small uncertainty (the gray band). Around that energy, the CFD result starts deviating towards slightly lower values of the phase, although it is still compatible with the UFD thanks to the fact that the uncertainty band becomes larger in that region.

This means that describing the data around the $K^*(892)$ resonance, whose mass is $\simeq$896 MeV and width is $\simeq$49 MeV, requires the phase in the 930 MeV to 1 GeV region to be somewhat below the existing data. We emphasize this remark because in the solution of the Roy-Steiner equations in [14], the $K^*(892)$ phase comes out somewhat incompatible with the data (we show the result as a dotted line in Fig. 19). To obtain such a solution the authors use as a boundary condition the value of the phase (and its derivative) at $\sqrt{s} = \sqrt{0.935\ \text{GeV}^2} \simeq 0.967$ GeV, which they take to be $155.8 \pm 0.4°$. However, at that energy, our CFD result yields $152.5 \pm 2.0°$. This could suggest that the mismatch between the Roy-Steiner solution of [14] and the scattering data around the $K^*(892)$ resonance could be due in part to the choice of matching phase and that it might be improved by lowering it by roughly 3°, as our CFD prefers.

In the threshold region we have calculated the scattering length directly from the CFD parametrization:

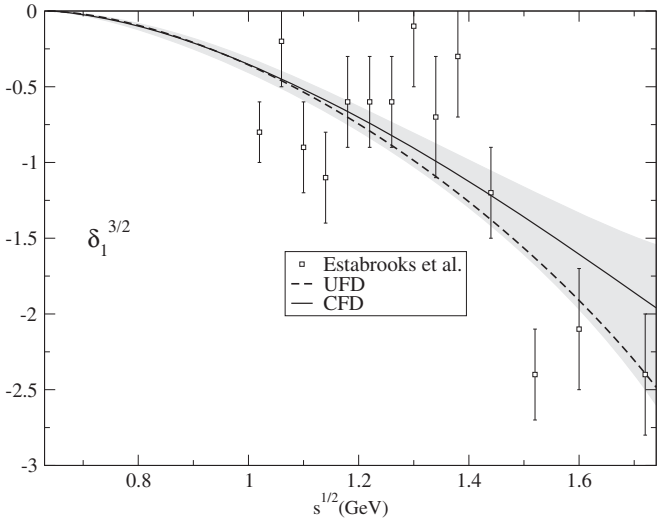

FIG. 18. Phase shift of the $P^{3/2}$ wave. Data are from [22]. We show as a continuous line the CFD fit and the gray band covers its uncertainties. The UFD result lies right on the border of this uncertainty band. Note that this phase is rather small up to 1.74 GeV.

$$m_\pi a_1^{1/2} = 0.024^{+0.008}_{-0.005}, \tag{59}$$

to be compared with the UFD result $m_\pi a_1^{1/2} = 0.031^{+0.013}_{-0.008}$. Note that since our UFD and CFD fits describe the data in Fig. 19, the resulting scattering lengths are larger than the one obtained in [14], $m_\pi a_1^{1/2} = 0.019 \pm 0.001$.

3. t_P wave

Once we have described both the isospin $1/2$ and $3/2$ P waves, we show the modulus and phase of the $t_P = t_1^{1/2} + t_1^{3/2}/2$ amplitude in Figs. 20 and 21, respectively. In the inelastic region both the phase and the modulus obtained for the CFD solution are compatible with the UFD parametrizations. Actually, by looking at Table VII one can check to see that the CFD parameters are almost identical to their UFD counterparts, varying by less than one deviation, except the a parameter, which changes by 1.4 deviations.

Our CFD solution describes fairly well the three resonances observed in this partial wave, namely, the $K^*(892)$, the $K^*(1410)$ and the $K^*(1680)$.

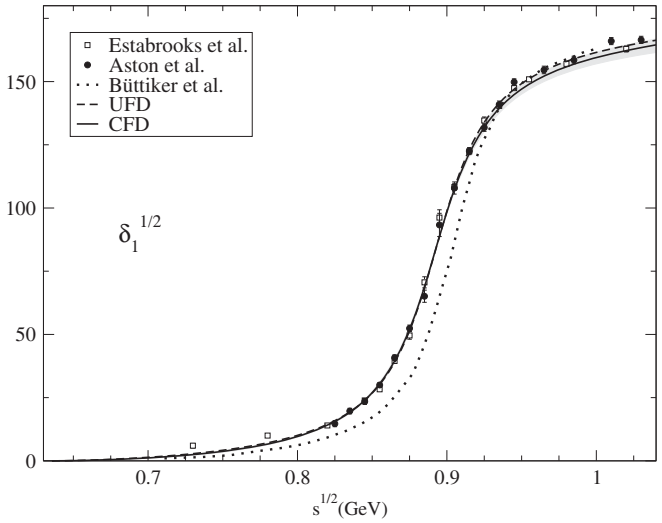

FIG. 19. Phase shift of the $P^{1/2}$ wave. The CFD and UFD results are almost indistinguishable up to 950 MeV, where the CFD phase becomes somewhat smaller. Note however that the UFD results still lie inside the uncertainty band. In addition we show the solution in [14]. Data are from [22,24].

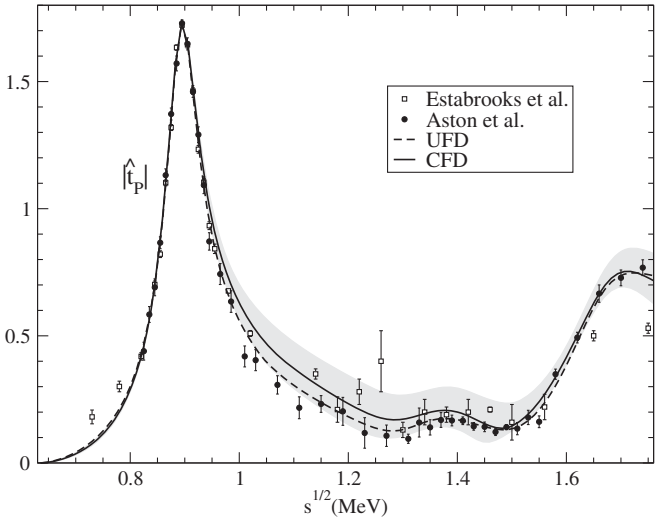

FIG. 20. Modulus of the $\hat{t}_P = \hat{t}_1^{1/2} + \hat{t}_1^{3/2}/2$ amplitude. We show the CFD fit as a continuous line and its uncertainty as a gray band. Note that the UFD result (dashed line) is also compatible within the CFD uncertainties. Data are from [22,24].

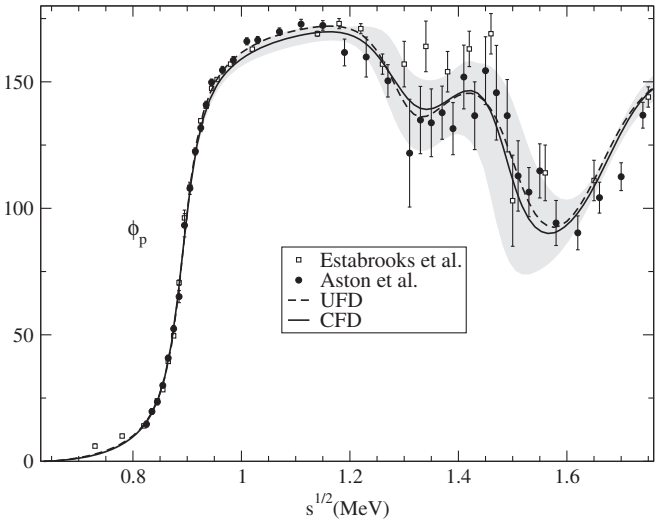

FIG. 21. Phase of the $t_P = t_1^{1/2} + t_1^{3/2}/2$ amplitude. We show the CFD fit as a continuous line and its uncertainty as a gray band. Note that the UFD result (the dashed line) is also very compatible within the CFD uncertainties. Data are from [22,24].

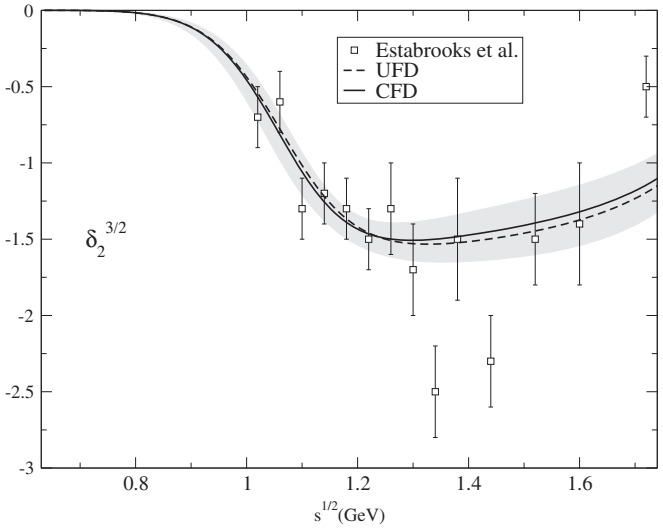

FIG. 22. $D^{3/2}$ phase shift. Data are from [22]. We show the CFD result as a continuous line and its uncertainty as a gray band. Note that it deviates very slightly from the UFD result (the dashed line) and only above 1.2 GeV.

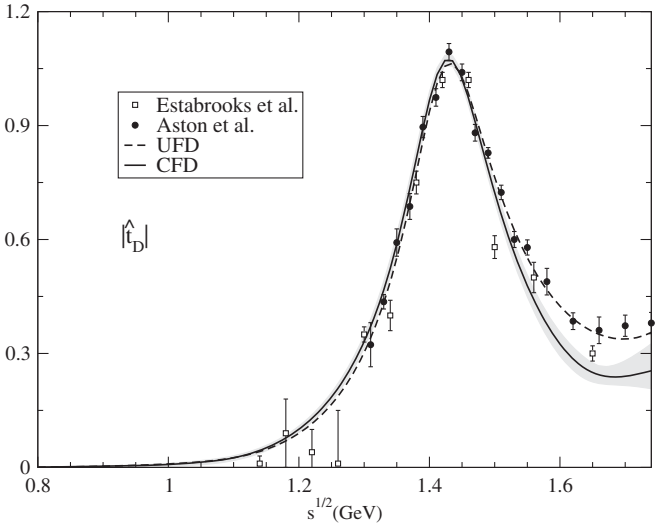

FIG. 23. Modulus of the $\hat{t}_D$ wave. Data are from [22,24]. Note the clear peak of the $K_2^*(1430)$ resonance and that above 1.6 GeV the UFD central result (the dashed line) is incompatible with the CFD result (the continuous line) within its uncertainties (the gray band).

Let us remark that although the two parametrizations are compatible, the CFD result prefers, for the modulus, the data of Estabrooks *et al.* [22] between 1 and 1.5 GeV.

D. D waves

1. $D^{3/2}$ wave

In Fig. 22 we show the CFD result for the $D^{3/2}$ wave, whose structure is relatively simple and whose size and influence are rather small, but not completely negligible, particularly in the inelastic regime. As seen in the figure, the CFD solution we obtain is almost the same as the UFD parametrization. In Table VIII it can be observed that the CFD parameters change by less than one third of a deviation from their UFD counterparts.

2. t_D wave

Since there are no data in the elastic region for the $I = 1/2$ D-wave partial wave, we directly show the modulus and phase of the $t_D = t_2^{1/2} + t_2^{3/2}/2$ combination in Figs. 23 and 24, respectively. For the modulus, the CFD solution is almost indistinguishable from the UFD curve up to 1.6 GeV. However, above that energy the central UFD value lies typically 2 to 3 deviations away from the central CFD value. Nevertheless, both fits are still compatible due to the rather large uncertainty band of the UFD set, shown in Fig. 9. Concerning the phase, this is the curve where, above 1.6 GeV, we find the largest deviation from the data and the UFD set. By comparing the CFD versus the UFD parameters for this wave, given in Table IX, we find that the ϕ_0 parameter changes by more than 3 deviations. This is the only parameter that changes so dramatically from its UFD to its CFD value. Note it is closely related to the background produced by the opening of the $K\eta$ channel.

This deviation is not too worrisome since it occurs at the very end of our parametrizations and outside the peak of the $K_2^*(1430)$, whose width is roughly 100 MeV. Therefore, the amplitude in that region is relatively small. At this point it is important to recall that the symmetric FDR, shown in Fig. 14, is well satisfied by the CFD set only up to 1.6 GeV. Above that energy, it improves the UFD result, but it is not enough to consider it satisfactory. As already commented,

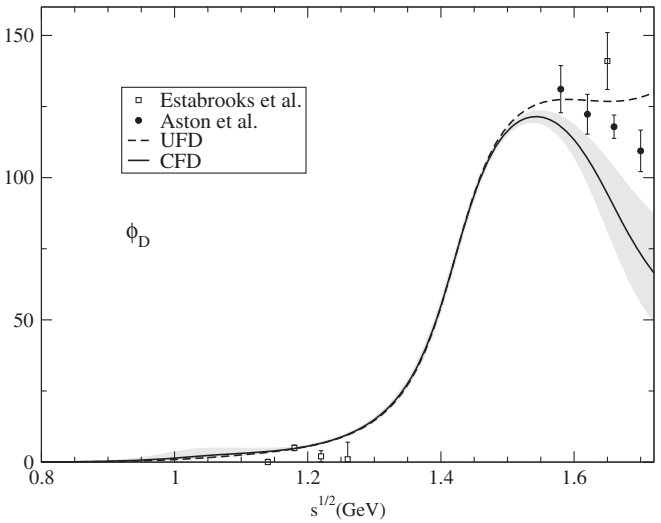

FIG. 24. Phase of the t_D wave. Data are from [22,24]. Note the sharp phase rise due to the $K_2^*(1430)$ resonance and that above 1.6 GeV the existing data and the UFD central result (the dashed line) are both incompatible with the CFD result (the continuous line) within its uncertainties (the gray band).

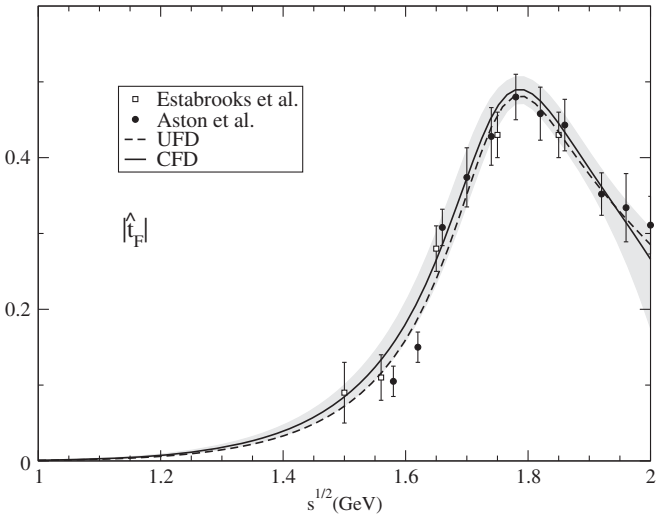

FIG. 25. Modulus of the $F^{1/2}$ wave. Data are from [22,24]. Note that the peak of the $K_3^*(1780)$ resonance is well described by both the CFD and UFD curves, which are very compatible. The gray band stands for the CFD uncertainty.

this is one of the reasons why in this work we claim to have precise and consistent data parametrizations up to 1.6 GeV and not beyond. Above that region the measured data is hard to reconcile with the dispersive constraints. This might be due to the existence of further systematic uncertainties, not necessarily in this wave, or to the increasingly important contribution from the tower of partial waves to the partial wave expansion.

E. $F^{1/2}$ wave

The CFD result for the $F^{1/2}$ wave is almost indistinguishable from our previous UFD result and describes nicely the $K_3^*(1780)$. This can be seen in Figs. 25 and 26,

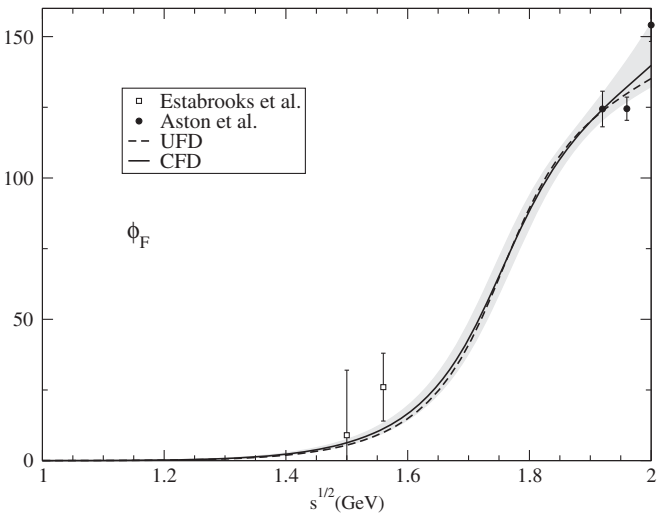

FIG. 26. Phase of the $F^{1/2}$ wave. Data are from [22,24]. Note that the CFD and UFD curves are very compatible. The gray band stands for the CFD uncertainty.

where we show the modulus and the phase of the partial wave, respectively.

F. CFD Regge parametrizations

When imposing dispersive constraints on the amplitude, we have also allowed the $f_{K/\pi}$, r and $g_{K/\pi}$ Regge parameters to vary. The rest of the Regge parameters have been kept fixed to the values in the literature, also used for the UFD set and given in Table XI. The reason is that, in principle, these other parameters can be determined without using processes involving kaons or πK scattering.

In Table XII we can observe that, in the end, the $f_{K/\pi}$ and r parameters barely change. However the CFD value of $g_{K/\pi}$ changes by 2.5 deviations from its UFD counterpart and is responsible for more than half of the reduction in $d_{T^-}^2$, particularly at high energies. As we commented before, it is not very surprising that this parameter suffers a large change, since there is little information to determine it reliably. It can be considered that in this work we are making a dispersive determination of this parameter.

VI. DISCUSSION

Before concluding, let us discuss our results in relation to data obtained from the decay of heavier particles, as well as regarding poles of resonances in the elastic regime and particularly the controversial $K_0^*(800)$ or κ meson.

A. Data from decays of heavier particles

As was already commented in Sec. III A, further information on the πK system has been obtained from the decays of heavier particles.

The semileptonic $D^+ \to K^-\pi^+e^+\nu_e$ decays have been analyzed by the *BABAR* [25] and BESIII [26] collaborations providing data on the phase difference between the S and P components. Since only the πK's interact strongly in the final state, Watson's theorem applies and in the elastic region this measurement is nothing but the difference between the S and P scattering phase shifts. In Fig. 27 we show the results for the $I = 1/2$ S-wave phase obtained from semileptonic D decays, compared to those from scattering experiments. Note that the uncertainties from decays are much larger than those obtained from scattering. Although what is actually measured in these decays is the phase-shift difference between the P and S waves, the experimental collaborations provide tables for the S wave alone, by using a simple P-wave description, whose uncertainty is much smaller and can be neglected. A similar procedure has been followed with the LASS scattering data of Aston *et al.* [24] shown in Fig. 27 for comparison, where the $I = 3/2$ component has been separated with the Estabrooks *et al.* model [22]. The above caveats and the very large uncertainties justify our not including data from decays in our fits. All in all, there is a nice qualitative agreement between different data sources and also with our

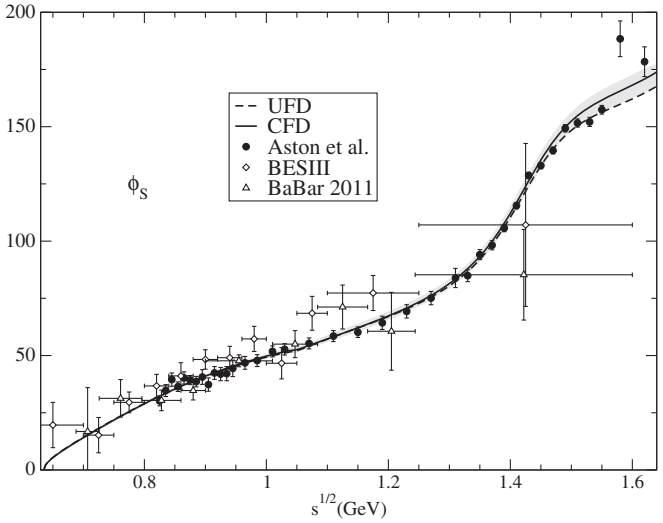

FIG. 27. Phase of the $I = 1/2$ πK S wave obtained from the semileptonic decay $D^+ \to K^-\pi^+e^+\nu_e$ by the *BABAR* Collaboration [25] and recently by the BESIII Collaboration [26]. These phases are compared to the LASS scattering phase shift of Aston *et al.* (using their $I = 3/2$ parametrization to separate the $I = 1/2$). Note that the experiments are in fairly good agreement up to 1.6 GeV.

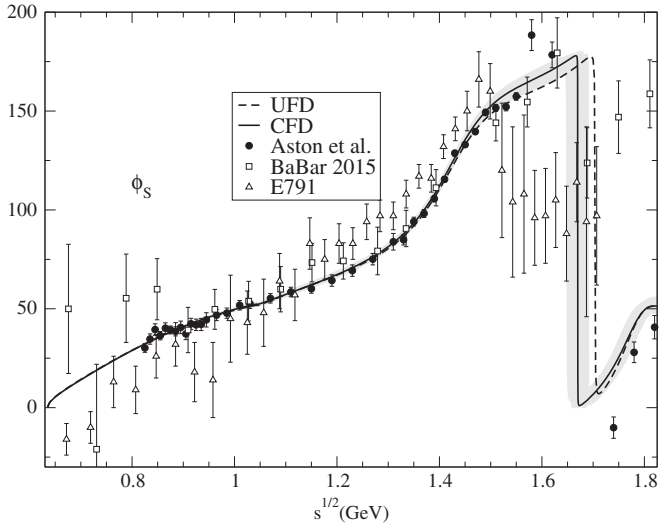

FIG. 28. Phase of the $I = 1/2$ πK S wave obtained from Dalitz plot analyses of $D \to K\pi\pi$ by the E791 Collaboration [27] and of $\eta_c \to K^0_S K^\pm\pi^\mp$ by the *BABAR* Collaboration [30]. We have plotted the systematic plus the statistical uncertainties for [27]. These phases are compared to the LASS scattering phase shift of Aston *et al.* (using their $I = 3/2$ parametrization to separate the $I = 1/2$). The data from *BABAR* are displaced by 34° while those from E791 are displaced by 86°. Note that the qualitative agreement with the scattering phase only reaches up to 1.5 GeV and is not particularly good at low energies.

UFD and CFD results that we also show in the figure. Moreover it is reassuring to see the good agreement between our parametrizations and the decay data in the near threshold region, where no scattering data exist.

In addition, from Dalitz plot analyses it has been possible to extract the $I = 1/2$ amplitude and phase of the πK S-wave component in $D^+ \to K^-\pi^+\pi^+$ by the E791 [27], FOCUS [28] and CLEO-c [29] collaborations, as well as in $\eta_c \to K\bar{K}\pi$ by the *BABAR* Collaboration [30]. As was already commented in Sec. III A, in this case Watson's theorem does not imply that the phase thus measured should be the same as that of scattering. The reason is the presence of another strongly interacting particle in the final state. This is particularly obvious by noting that the measured amplitudes and phases do not satisfy the elastic scattering unitarity condition. Nevertheless, it has also been noticed in these works that the measured phase shows a qualitative agreement with the scattering phase shift in the elastic region, once it is appropriately displaced by a constant. We show this qualitative agreement in Fig. 28, where once again the data from scattering has been extracted using the simple $I = 3/2$ model suggested by the experimental authors, which is a good enough description for a qualitative comparison. Once more, our UFD and CFD parametrizations describe well all these data.

Note, however, that the agreement disappears in the region above 1.6 GeV, which is where we have also found that the scattering data are largely incompatible with forward dispersion relations. It is then tempting to fit in this region the phase from decays instead of the phase from scattering, in the hope that the FDRs may be better satisfied. However, note that we can only try to fit the phase from decays, based on its similarity to the scattering phase, but not the modulus, since the energy dependence observed for the latter is very different from that of scattering. We have performed this exercise and we have verified that the FDRs are satisfied even more poorly.

B. Pole parameters of elastic resonances

Our partial waves are constructed as piecewise parametrizations which are matched continuously in the real axis. As a consequence, the resulting global amplitude does not provide a rigorous analytic continuation to the whole complex plane. Each one of the pieces may have an analytic continuation of its own, but at most it may only be a good approximation to the amplitude near the part of the real axis where that particular function is used, far from the other pieces of functions. Nevertheless, in the elastic region we have used a conformal mapping which has a well-defined analytic continuation to the complex s plane. As explained in Appendix A, the interesting feature of this mapping is that it places the inelastic singularities at the boundary of the unit circle. Therefore one can expect that it will provide a relatively good representation of the partial wave for complex values of s which are not close to that boundary.

With these caveats in mind, we can obtain a determination of the pole positions of resonances that appear in the elastic region by considering the analytic continuation of

just the elastic conformal parametrizations. Two such resonances exist, both with $I = 1/2$, namely, the controversial $K_0^*(800)$, or κ meson, and the $K^*(892)$ in the scalar and vector partial waves, respectively. Their associated poles are located in the second Riemann sheet of the partial wave, defined as

$$t^{II}(s) = \frac{t(s)}{1 + 2i\sigma(s)t(s)}, \tag{60}$$

where in the upper half complex s plane $\sigma(s)$ is defined as in Sec. II, whereas in the lower half plane $\sigma(s) = -\sigma(s^*)^*$. Therefore the second sheet pole position is a solution of

$$\cot\delta_l^I(s_{\rm pole}) = -i, \tag{61}$$

where the analytic continuation of the cotangent of the phase shift is obtained through the conformal expansion in Eqs. (13) and (28) for the $K_0^*(800)$ and the $K^*(892)$, respectively.

Customarily, since for narrow resonances isolated from other poles or thresholds the Breit-Wigner formula applies, one identifies the pole position of a resonance with its mass and width as follows: $s_R = (M_R - i\Gamma_R/2)^2$. Despite the $K_0^*(800)$ being a very wide resonance, we keep this convention and the resulting pole parameters for this resonance can be found in Table XV, both for the UFD and the CFD parametrization. This is also the convention used in the Review of Particle Physics (RPP) [16]. The values we obtain are very compatible with the averaged mass in the RPP, $M_{K_0^*(800)} = 682 \pm 29$ MeV. In contrast, the width is somewhat larger than the value quoted there, $\Gamma_{K_0^*(800)} = 547 \pm 24$ MeV. Actually, the most rigorous derivation is that in [13] by means of a Roy-Steiner analysis, where it is found that $M_{K_0^*(800)} = 658 \pm 13$ MeV and $\Gamma_{K_0^*(800)} = 557 \pm 24$ MeV. Nevertheless, there is a large spread of values listed in the RPP and several other determinations find a width very similar to ours. As a word of caution, when making a comparison to the RPP one should take into account that our numbers correspond to a pole position, whereas many values there correspond to peak parametrizations through Breit-Wigner formalisms or its variations, whose applicability is dubious due to the large width of this resonance.

The corresponding poles for the vector $K^*(892)$ are found in Table XVI. In this case the pole mass is very similar to the values provided in the RPP, typically obtained from Breit-Wigner parametrizations. In contrast our pole width is about 10 MeV higher that the ones listed in the RPP or those found in $\tau^- \to K_S\pi^-\nu_\tau$ decays by the Belle Collaboration [46] and on $D^+ \to K^-\pi^+e^+\nu_e$ decays by the *BABAR* Collaboration [25]. It has been pointed out in [47] that this shift may occur on the width when fitting the LASS Collaboration [24] phase shift due to the fact that those data have been given before unfolding the detector mass resolution, yielding 56 MeV instead of the 50.8 MeV quoted in the original LASS publication [24]. A similar caveat is pointed out by Estabrooks *et al.* [22], who estimate a ±5 MeV systematic uncertainty in their width determination for this reason. In both cases it is pointed out that this effect barely affects the mass determination. Of course, all these experimental poles have been extracted by using Breit-Wigner parametrizations modified with Blatt-Weiskopf barrier factors, which are also model dependent.

TABLE XV. Pole parameters of the $K_0^*(800)$ from the analytic continuation of the elastic parametrization only.

Poles	Mass (MeV)	Width (MeV)	Coupling
UFD	673 ± 15	674 ± 15	5.01 ± 0.07
CFD	680 ± 15	668 ± 15	4.99 ± 0.08

TABLE XVI. Pole parameters of the $K^*(892)$ from the analytic continuation of the elastic parametrization only.

Poles	Mass (MeV)	Width (MeV)	Coupling
UFD	893 ± 1	56 ± 2	5.95 ± 0.07
CFD	892 ± 1	58 ± 2	6.02 ± 0.06

For the future, we plan to impose consistency with partial wave dispersion relations starting from the parametrizations we have obtained in this work. Those dispersion relations will provide a rigorous analytic continuation to the complex plane and a rigorous and precise determination of the resonance poles. In addition, we plan to use a simpler but model-independent method, recently proposed to extract the poles from the knowledge of scattering data in the real axis by means of Padé approximants and Montessus's theorem [48]. These two approaches are beyond the scope of the present work, which is only focused on obtaining a data description consistent with FDRs.

VII. CONCLUSIONS AND OUTLOOK

In this work we have presented a set of pion-kaon scattering parametrizations, which up to 1.6 GeV describe data and simultaneously satisfy a complete set of forward dispersion relations as well as three sum rules for threshold parameters. Our aim has been to make the parametrizations relatively simple and easy to implement in future theoretical or experimental applications.

As a first step we have obtained a set of UFD, in which partial waves with different angular momenta are fitted independently. Waves with different isospins are fitted together because that is how data was originally obtained. We have paid particular attention to the estimation of uncertainties, particularly to those of a systematic nature, which are not always taken into account in the literature. In addition, for the most controversial wave we have checked some statistical tests for the consistency of our uncertainty

estimates. Above 1.74 GeV, since no data on all partial waves exist, we have used Regge parametrizations that were obtained in previous works by applying factorization to other processes involving nucleons, pions and kaons.

However, it is shown that, even within uncertainties, this UFD set does not satisfy well forward dispersion relations and also shows some tension when used inside the threshold sum rules. In particular, above the $K\eta$ threshold the dispersive results lie typically 2 deviations or more away from the direct calculation when using the UFD parametrizations. Throughout the elastic region the agreement is somewhat better, but still only at the level of 1.5 deviations.

Thus, as a second step, we have imposed the forward dispersion relations and the sum rules as constraints on the fit parameters. Note that the parametrizations stay the same and we only change the values of the parameters. Our final result is a set of CFD that satisfies forward dispersion relations remarkably well up to 1.6 GeV while still describing the data. In particular, the deviations between the CFD and UFD results have been shown to be relatively small and within the uncertainties of the UFD fit. As a consequence, the CFD set still provides a good description of the data. Above 1.6 GeV, we have found that the fulfillment of the dispersive constraints would require large modifications of the fits that would spoil the data description. Thus our parametrizations describe the data and are simultaneously consistent with dispersive constraints only up to 1.6 GeV.

Using this CFD set we have provided a precise determination of three combinations of scattering lengths and slope parameters. In addition, given that the conformal map parametrization chosen for the elastic region has very good analytic properties in the complex plane we have obtained the pole parameters of the resonances that appear in that region, namely the vector $K^*(892)$ and the controversial scalar $K_0^*(800)$ or κ meson. The poles and residues come in reasonably good agreement with previous determinations, although, of course, the analytic continuation is dependent on our choice of conformal mapping, which is very reasonable, but not entirely model independent. Nevertheless, we plan to use our CFD results in the real axis as input to extract pole parameters using model-independent analytic approaches.

For the future we also plan to constrain further our parametrizations with a complete set of equations of the Roy-Steiner type. These are much more complicated relations written in terms of partial waves but they are very relevant to imposing crossing in addition to analyticity. Also, being formulated in terms of partial waves, they allow for a rigorous continuation to the complex plane, independent of the parametrizations used in the real axis. Thus they can provide a rigorous determination of the parameters of the resonances. Nevertheless, unlike the forward dispersion relations used here, they are limited in practice to roughly the elastic region. Moreover, equations of the Roy-Steiner type use as input the amplitudes in the whole energy region, for which it is important to use as input the CFD set obtained here.

We also expect that the simple parametrization of all the relevant partial waves can be of use in present and future experimental and theoretical analysis involving pions and kaons in the final state.

ACKNOWLEDGMENTS

J. R. P. and A. R. are supported by Spanish Projects No. FPA2011-27853-C02-02 and No. FPA2014-53375-C2-2 and Red de Excelencia de Física Hadrónica FIS2014-57026-REDT. We are very grateful to B. Moussallam for kindly providing us with his parametrizations as well as for his instructive comments and discussions.

APPENDIX A: CONFORMAL EXPANSION FOR ELASTIC WAVES

Let us recall that elastic partial waves can be written as

$$t_l(s) = \frac{1}{\sigma(s)} \frac{1}{\cot \delta_l(s) - i}, \tag{A1}$$

where $\sigma(s) = 2q/\sqrt{s}$ and q is the center of mass momentum. In the complex s plane, partial waves for the scattering of two particles with different masses m_1 and m_2 have a distinct analytic structure in the first Riemann sheet, shown in Fig. 29(a). First of all, there is a right-hand or physical cut extending from the opening of the elastic threshold to infinity. In addition, due to the thresholds in the crossed channels, there is a left-hand cut extending from $(m_1 - m_2)^2$ to $-\infty$, as well as a circular cut at $|s|^2 = (m_1^2 - m_2^2)^2$. Other singularities may appear on the real axis when bound states exist in the direct or crossed channels, but this is not the case in πK scattering. Let us emphasize that there are no poles in the first Riemann sheet. The cut singularities are reproduced in the second Riemann sheet, where poles can now occur anywhere in the complex plane. When poles are sufficiently close to the real axis, they give rise to resonant phenomena.

Now, in order to describe the amplitude in the complex s plane, it is customary to recast the partial wave as

$$t_l(s) = \frac{q^{2l}}{\Phi(s) - iq^{2l}\sigma(s)}, \tag{A2}$$

so that, as shown in Fig. 29(b), the effective range function $\Phi(s)$ does not have elastic cuts, but only the left-hand and circular ones, as well as the inelastic cuts. Depending on the dynamics, it might also have poles at the zeros of the amplitude, as we will discuss below. In our case, it has no singularity from the πK threshold to the next inelastic

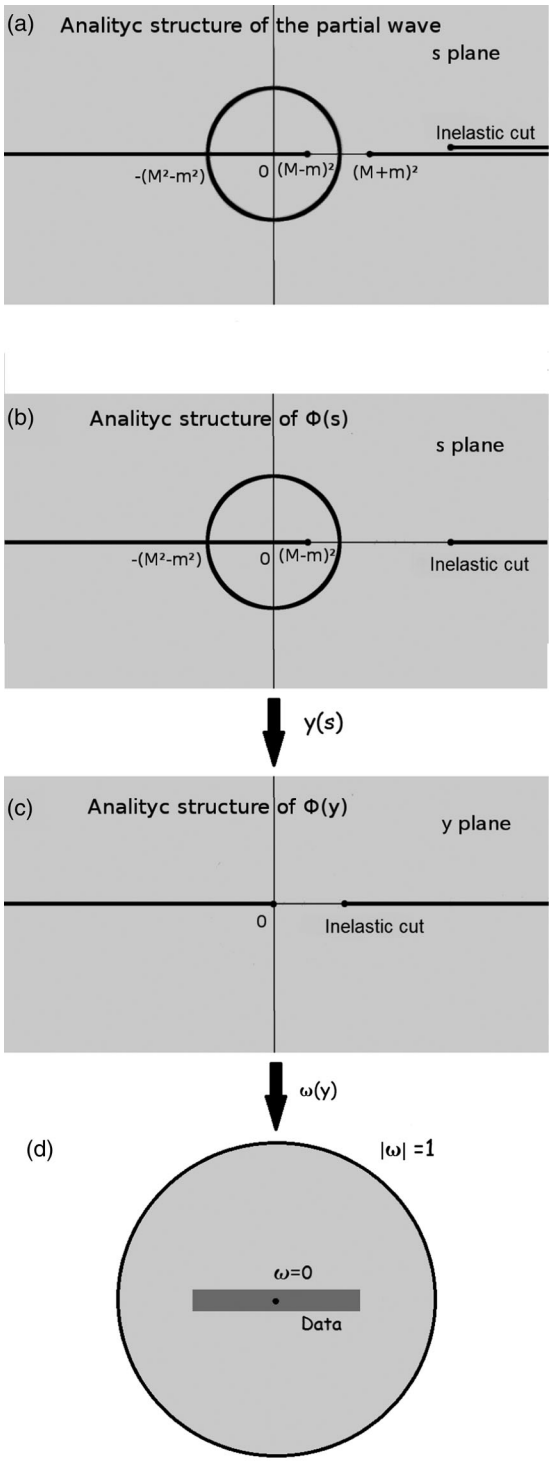

FIG. 29. Analytic structure in different variables of a πK scattering partial wave $t(s)$ and effective range function $\Phi(s)$: (a) $t(s)$ in the complex s plane. Note the elastic, inelastic, left-hand and circular cuts. (b) $\Phi(s)$ in the s plane has the same structure as $t(s)$ except for the absence of the elastic cut. (c) In the $y(s)$ plane the circular cut disappears. (d) The conformal variable $\omega(y)$ maps the whole analyticity domain of $\Phi(y)$ inside the unit circle, whereas the cut singularities are confined to $|\omega| = 1$. Note that ω is defined so that the data region is roughly centered around $\omega = 0$ and not too close to the border.

threshold s_0. When the expansion of $\Phi(s)$ is made in terms of the powers of q, the coefficient of the first term of the expansion is known as the scattering length, the second is the slope, etc. But the radius of convergence of this series, centered at $s = (m_K + m_\pi)^2$, is small, since the circular cut singularity lies rather close. The best way to use the largest possible domain of analyticity is by changing variables by means of a conformal transformation. In this case, however, it is convenient to perform first another change of variable which maps the circular cut into the left real axis:

$$y(s) = \left(\frac{s - \Delta_{K\pi}}{s + \Delta_{K\pi}}\right)^2, \tag{A3}$$

where $\Delta_{K\pi} = m_K^2 - m_\pi^2$. The resulting $\Phi(y(s))$ function now only has a right-hand "inelastic" cut and a left-hand cut, as shown in Fig. 29(c), and then we can use the conformal variable

$$w(y) = \frac{\sqrt{y} - \alpha\sqrt{y_0 - y}}{\sqrt{y} + \alpha\sqrt{y_0 - y}}, \tag{A4}$$

to map the cut y plane into the unit circle in the ω plane.

With the exception of the minute $P^{3/2}$ and $D^{3/2}$ waves, in this work we have chosen α for each wave so that the center of the conformal expansion $\omega = 0$ corresponds to the intermediate point between the πK threshold and the energy of the last data point that is fitted with the conformal formula. The reason for this choice is to ensure that the region where data is to be fitted lies well inside the ω circle, roughly centered around $\omega = 0$, as shown in Fig. 29(d). Actually, for the $S^{1/2}$ and $P^{1/2}$ waves, the data fitted with the elastic formalism lie at $|\omega| < 0.45$. However for the $S^{3/2}$ wave the data lie at $|\omega| < 0.6$. The $P^{3/2}$ and $D^{3/2}$ waves are an exception, because their data starts at 1 GeV, far from the πK threshold. Thus we have chosen their α parameters so that the center of the conformal expansion corresponds to the intermediate point where data exists. With this choice, the data fitted with this conformal expansion lies at $|\omega| < 0.6$.

Since with these changes of variable the singularities now lie at $|\omega| = 1$, the function has an analytic expansion $\Phi(s) = \sum_n B_n w(s)^n$ convergent in the whole $|\omega| < 1$ circle. In this way, and in terms of s, the domain of analyticity of the conformal mapping extends to the whole complex plane outside the circular cut, with a left-hand cut and a right-hand cut above the first inelastic threshold. Thus on the elastic region of the real axis

$$\cot\delta_l(s) = \frac{\sqrt{s}}{2q^{2l+1}}\Phi(s) = \frac{\sqrt{s}}{2q^{2l+1}}\sum_n B_n w(s)^n, \tag{A5}$$

which are the expressions we have used for our elastic fits.

Finally, let us recall that due to chiral symmetry, scalar partial waves have a so-called Adler zero below threshold,

which is easily implemented in the partial waves by writing a pole factor in front of the $\Phi(s)$ expansion, as follows:

$$\Phi(s) = \frac{1}{s - s_{\rm Adler}} \sum_n B_n w(s)^n. \tag{A6}$$

In addition, when there is a narrow well-established resonance and the phase crosses $\pi/2$ at m_r it is also convenient to extract a factor out of the conformal expansion as

$$\Phi(s) = (s - m_r^2) \sum_n B_n w(s)^n, \tag{A7}$$

to accelerate the convergence of the fit.

APPENDIX B: STATISTICAL TEST ON THE S WAVE

Since the $S^{1/2}$ wave is the most controversial one, we have used some statistical tests to check the consistency of our fits and the data obtained from [22] and [24] for the $t_S \equiv t_0^{1/2} + t_0^{3/2}/2$ amplitude. As has been explained in the main text, the problem with the data is the existence of large systematic uncertainties that we necessarily had to estimate. Once we had these systematic uncertainties added to the statistical ones, we have performed the fits and obtained, by minimizing the χ^2, the fit parameters and their uncertainties. The χ^2 is based on a Gaussianity assumption and one would like to test to see that the resulting fit and the data are still consistent with it. For this reason we will check the consistency of our fits by means of the central moment statistical test, which in rather similar conditions was suggested for $\pi\pi$ scattering in [32].

Let N be the number of data points, measured at energies $\sqrt{s_i}$, $i = 1 \ldots N$. We then introduce a set of N residuals $R_i = (P_i - f(\alpha, s_i))/(\Delta P_i)$. Here P_i is the experimental value of the ith measurement, ΔP_i its uncertainty (experimental and systematic) associated with that value, and $f(\alpha, s_i)$ is the theoretical model evaluated at s_i. The set of UFD parameters is called α.

By assumption, this set of residuals must obey a standardized normal distribution. For this purpose we study the central moments of the residual distribution

$$\mu_{UFD,n} = \frac{1}{N} \sum_{i=1}^{N} (R_i - R_{\rm mean})^n, \tag{B1}$$

where $R_{\rm mean} = \sum R_i/N$.

We would like to compare these $\mu_{UFD,n}$ with the expected value of a set of N data standardized Gaussian points. Thus, we generate M samples of distributions of N data points R_{ik}, $k = 1, \ldots M$ that follow a normal Gaussian distribution, and calculate the central moments μ_{nk} of each sample. We then define the average central moment $\langle \mu_n \rangle = \sum_k^M \mu_{nk}/M$. Similarly, we define the uncertainty in this distribution of residuals as the usual standard deviation: $\Delta\mu_n \equiv \sqrt{\langle \mu_n^2 \rangle - \langle \mu_n \rangle^2}$.

In order to compare the moments of our UFD result with those of the generated distributions, we have to recall that we have parametrized the S wave into two regions with different functional forms, and we have fitted two sets of observables, $|\hat{t}_S|$ and ϕ_S. Therefore we have four different tests, which are presented in Tables XVII, XVIII, XIX and XX.

Actually, our procedure to estimate uncertainties has made use of these tests. At first we introduce as systematic uncertainties half of the distance between those points measured at the same energy which are incompatible. Then, we modify the systematic uncertainties of the few data points that cause deviations from the Gaussian behavior of the tests. With these modified systematic uncertainties the fit is performed again, the tests are checked once more and the systematic uncertainties of points that cause deviations from the test are changed again. The procedure is iterated until the Gaussianity tests are well satisfied.

TABLE XVII. Normality condition for Φ_S in the elastic region.

n	1	2	3	4	5	6
$\mu_{\rm UFD},n$	0	0.8	−0.3	1.6	−1.1	4.2
$\mu_{\rm random},n$	0 ± 0	1.0 ± 0.2	0 ± 0.4	2.8 ± 1.6	0 ± 4	14 ± 17

TABLE XVIII. Normality condition for $|\hat{t}_S|$ in the elastic region.

n	1	2	3	4	5	6
$\mu_{\rm UFD},n$	0	1.1	0.1	2.4	0.8	6.7
$\mu_{\rm random},n$	0 ± 0	1.0 ± 0.2	0 ± 0.4	2.8 ± 1.6	0 ± 4	14 ± 17

TABLE XIX. Normality condition for the Φ_S in the inelastic region.

n	1	2	3	4	5	6
$\mu_{\rm UFD},n$	0	1	0.2	3.3	−2.1	18.1
$\mu_{\rm random},n$	0 ± 0	1.0 ± 0.2	0 ± 0.4	2.8 ± 1.6	0 ± 4	14 ± 16

TABLE XX. Normality condition for the $|\hat{t}_S|$ in the inelastic region.

n	1	2	3	4	5	6
$\mu_{\rm UFD},n$	0	0.9	0.09	1.6	0.6	3.6
$\mu_{\rm random},n$	0 ± 0	1.0 ± 0.2	0 ± 0.4	2.8 ± 1.6	0 ± 4	14 ± 16

[1] J. Gasser and H. Leutwyler, Chiral perturbation theory: Expansions in the mass of the strange quark, Nucl. Phys. **B250**, 465 (1985).

[2] V. Bernard, N. Kaiser, and U. G. Meissner, πK scattering in chiral perturbation theory to one loop, Nucl. Phys. **B357**, 129 (1991).

[3] J. Bijnens, P. Dhonte, and P. Talavera, πK scattering in three flavor ChPT, J. High Energy Phys. 05 (2004) 036.

[4] B. Ananthanarayan, P. Büttiker, and B. Moussallam, πK sum rules and the SU(3) chiral expansion, Eur. Phys. J. C **22**, 133 (2001); B. Ananthanarayan and P. Büttiker, Comparison of pion kaon scattering in SU(3) chiral perturbation theory and dispersion relations, Eur. Phys. J. C **19**, 517 (2001).

[5] A. Dobado and J. R. Pelaez, A global fit of $\pi\pi$ and πK elastic scattering in ChPT with dispersion relations, Phys. Rev. D **47**, 4883 (1993); A. G. Nicola and J. R. Pelaez, Meson-meson scattering within one-loop chiral perturbation theory and its unitarization, Phys. Rev. D **65**, 054009 (2002).

[6] J. R. Pelaez, Light scalars as tetraquarks or two-meson states from large N_c and unitarized chiral perturbation theory, Mod. Phys. Lett. A **19**, 2879 (2004).

[7] J. A. Oller and E. Oset, Chiral symmetry amplitudes in the S-wave isoscalar and isovector channels and the σ, $f_0(980)$, $a_0(980)$ scalar mesons, Nucl. Phys. **A620**, 438 (1997); **A652**, 407(E) (1999); N/D description of two meson amplitudes and chiral symmetry, Phys. Rev. D **60**, 074023 (1999); J. A. Oller, E. Oset, and J. R. Pelaez, Nonperturbative Approach to Effective Chiral Lagrangians and Meson Interactions, Phys. Rev. Lett. **80**, 3452 (1998); Meson-meson interaction in a nonperturbative chiral approach, Phys. Rev. D **59**, 074001 (1999); **60**, 099906(E) (1999); **75**, 099903(E) (2007).

[8] S. R. Beane, P. F. Bedaque, T. C. Luu, K. Orginos, E. Pallante, A. Parreño, and M. J. Savage, πK scattering in full QCD with domain-wall valence quarks, Phys. Rev. D **74**, 114503 (2006); J. Nagata, S. Muroya, and A. Nakamura, Lattice study of $K\pi$ scattering in $I = 3/2$ and $1/2$, Phys. Rev. C **80**, 045203 (2009); **84**, 019904(E) (2011); Z. Fu, Lattice study on πK scattering with moving wall source, Phys. Rev. D **85**, 074501 (2012); K. Sasaki, N. Ishizuka, M. Oka, and T. Yamazaki (PACS-CS Collaboration), Scattering lengths for two pseudoscalar meson systems, Phys. Rev. D **89**, 054502 (2014).

[9] C. B. Lang, L. Leskovec, D. Mohler, and S. Prelovsek, $K\pi$ scattering for isospin $1/2$ and $3/2$ in lattice QCD, Phys. Rev. D **86**, 054508 (2012); S. Prelovsek, L. Leskovec, C. B. Lang, and D. Mohler, $K\pi$ scattering and the K^* decay width from lattice QCD, Phys. Rev. D **88**, 054508 (2013); Z. Fu and K. Fu, Lattice QCD study on $K^*(892)$ meson decay width, Phys. Rev. D **86**, 094507 (2012); J. J. Dudek, R. G. Edwards, C. E. Thomas, and D. J. Wilson (Hadron Spectrum Collaboration), Resonances in Coupled $\pi K - \eta K$ Scattering from Quantum Chromodynamics, Phys. Rev. Lett. **113**, 182001 (2014); D. J. Wilson, J. J. Dudek, R. G. Edwards, and C. E. Thomas, Resonances in coupled $\pi K, \eta K$ scattering from lattice QCD, Phys. Rev. D **91**, 054008 (2015).

[10] M. Doring and U. G. Meissner, Finite volume effects in pion-kaon scattering and reconstruction of the $\kappa(800)$ resonance, J. High Energy Phys. 01 (2012) 009; M. Doring, U. G. Meissner, E. Oset, and A. Rusetsky, Scalar mesons moving in a finite volume and the role of partial wave mixing, Eur. Phys. J. A **48**, 114 (2012).

[11] R. L. Jaffe, Multiquark hadrons. I. Phenomenology of Q^2Q^{-2} mesons, Phys. Rev. D **15**, 267 (1977); M. D. Scadron, Spontaneous breakdown and the scalar nonet, Phys. Rev. D **26**, 239 (1982); E. van Beveren, T. A. Rijken, K. Metzger, C. Dullemond, G. Rupp, and J. E. Ribeiro, A low lying scalar meson nonet in a unitarized meson model, Z. Phys. C **30**, 615 (1986); R. Kaminski, L. Lesniak, and B. Loiseau, Three channel model of meson meson scattering and scalar meson spectroscopy, Phys. Lett. B **413**, 130 (1997); D. Black, A. H. Fariborz, F. Sannino, and J. Schechter, Putative light scalar nonet, Phys. Rev. D **59**, 074026 (1999); F. E. Close and N. A. Tornqvist, Scalar mesons above and below 1 GeV, J. Phys. G **28**, R249 (2002); A. H. Fariborz, E. Pourjafarabadi, S. Zarepour, and S. M. Zebarjad, Chiral nonet mixing in πK scattering, Phys. Rev. D **92**, 113002 (2015); T. Wolkanowski, M. Soltysiak, and F. Giacosa, $K_0^*(800)$ as a companion pole of $K_0^*(1430)$, arXiv:1512.01071.

[12] S. N. Cherry and M. R. Pennington, There is no $\kappa(900)$, Nucl. Phys. **A688**, 823 (2001).

[13] S. Descotes-Genon and B. Moussallam, The $K_0^*(800)$ scalar resonance from Roy-Steiner representations of πK scattering, Eur. Phys. J. C **48**, 553 (2006).

[14] P. Büttiker, S. Descotes-Genon, and B. Moussallam, A new analysis of πK scattering from Roy and Steiner type equations, Eur. Phys. J. C **33**, 409 (2004).

[15] F. Steiner, Partial wave crossing relations for meson-baryon scattering, Fortschr. Phys. **19**, 115 (1971).

[16] K. A. Olive (Particle Data Group), Review of particle physics, Chin. Phys. C **38**, 090001 (2014) and 2015 update.

[17] J. R. Pelaez and F. J. Yndurain, Pion-pion scattering amplitude, Phys. Rev. D **71**, 074016 (2005).

[18] Y. Cho *et al.*, Study of $K^-\pi^-$ scattering using the reaction $K^-d \to K^-\pi^- pp_s$, Phys. Lett. B **32**, 409 (1970).

[19] A. M. Bakker *et al.*, A determination of the $I = 3/2$ $K\pi$ elastic-scattering cross section from the reaction $K^-n \to pK^-\pi^-$ at 3 GeV/c, Nucl. Phys. **B24**, 211 (1970).

[20] B. Jongejans, R. A. van Meurs, A. G. Tenner, H. Voorthuis, P. M. Heinen, W. J. Metzger, H. G. J. M. Tiecke, and R. T. Van de Walle, Study of the $I = 3/2$ $K^-\pi^-$ elastic scattering from the reaction $K^-p \to K^-\pi^- p\pi^+$ at 4.25 GeV/c incident K^- momentum, Nucl. Phys. **B67**, 381 (1973).

[21] D. Linglin *et al.*, $K^-\pi^-$ elastic scattering cross-section measured in 14.3 GeV/c K^-p interactions, Nucl. Phys. **B57**, 64 (1973).

[22] P. Estabrooks, R. K. Carnegie, A. D. Martin, W. M. Dunwoodie, T. A. Lasinski, and D. W. G. S. Leith, Study of $K\pi$ scattering using the reactions $K^{+-}p \to K^{+-}\pi^+ n$ and $K^{+-}p \to K^{+-}\pi^-\Delta^{++}$ at 13 GeV/c, Nucl. Phys. **B133**, 490 (1978).

[23] R. Mercer *et al.*, $K\pi$ scattering phase shifts determined from the reactions $K^+p \to K^+\pi^-\delta^{++}$ and $K^0\pi^0\Delta^{++}$, Nucl. Phys. **B32**, 381 (1971).

[24] D. Aston *et al.*, A study of $K^-\pi^+$ scattering in the reaction $K^-p \to K^-\pi^+ n$ at 11 GeV/c, Nucl. Phys. **B296**, 493 (1988).

[25] P. del Amo Sanchez *et al.* (*BABAR* Collaboration), Analysis of the $D^+ \to K^-\pi^+e^+\nu_e$ decay channel, Phys. Rev. D **83**, 072001 (2011).

[26] M. Ablikim *et al.* (BESIII Collaboration), Study of $D^+ \to K^-\pi^+e^+\nu_e$, arXiv:1512.08627.
[27] E. M. Aitala *et al.* (E791 Collaboration), Model independent measurement of S-wave $K^-\pi^+$ systems using $D^+ \to K\pi\pi$ decays from Fermilab E791, Phys. Rev. D **73**, 032004 (2006); **74**, 059901(E) (2006).
[28] J. M. Link *et al.* (FOCUS Collaboration), Dalitz plot analysis of the $D^+ \to K^-\pi^+\pi^+$ decay in the FOCUS experiment, Phys. Lett. B **653**, 1 (2007); The $K^-\pi^+$ S-wave from the $D^+ \to K^-\pi^+\pi^+$ decay, Phys. Lett. B **681**, 14 (2009).
[29] G. Bonvicini *et al.* (CLEO Collaboration), Dalitz plot analysis of the $D^+ \to K^-\pi^+\pi^+$ decay, Phys. Rev. D **78**, 052001 (2008).
[30] J. P. Lees *et al.* (*BABAR* Collaboration), Measurement of the $I = 1/2$ $K\pi\mathcal{S}$-wave amplitude from Dalitz plot analyses of $\eta_c \to K\bar{K}\pi$ in two-photon interactions, Phys. Rev. D **93**, 012005 (2016).
[31] We thank B. Moussallam for kindly providing us with his parametrizations.
[32] R. N. Pérez, E. R. Arriola, and J. R. de Elvira, Self-consistent statistical error analysis of $\pi\pi$ scattering, Phys. Rev. D **91**, 074014 (2015).
[33] D. V. Bugg, Update on the kappa, Phys. Rev. D **81**, 014002 (2010).
[34] Z. Y. Zhou and H. Q. Zheng, An improved study of the kappa resonance and the non-exotic s wave πK scatterings up to $\sqrt{s} = 2.1$ GeV of LASS data, Nucl. Phys. **A775**, 212 (2006).
[35] S. Ishida, M. Ishida, T. Ishida, K. Takamatsu, and T. Tsuru, Analysis of $K\pi$ scattering phase shift and existence of $\kappa(900)$ particle, Prog. Theor. Phys. **98**, 621 (1997).
[36] M. Jamin, J. A. Oller, and A. Pich, S wave $K\pi$ scattering in chiral perturbation theory with resonances, Nucl. Phys. **B587**, 331 (2000).
[37] A. Dobado and J. R. Pelaez, Inverse amplitude method in chiral perturbation theory, Phys. Rev. D **56**, 3057 (1997).
[38] B. Adeva *et al.* (DIRAC Collaboration), First πK atom lifetime and πK scattering length measurements, Phys. Lett. B **735**, 288 (2014).
[39] P. Guo, R. Mitchell, M. Shepherd, and A. P. Szczepaniak, Amplitudes for the analysis of the decay $J/\psi \to K^+K^-\pi^0$, Phys. Rev. D **85**, 056003 (2012).
[40] R. Garcia-Martin, R. Kaminski, J. R. Pelaez, J. Ruiz de Elvira, and F. J. Yndurain, Pion-pion scattering amplitude. IV. Improved analysis with once subtracted Roy-like equations up to 1100 MeV, Phys. Rev. D **83**, 074004 (2011).
[41] J. P. Ader, C. Meyers, and B. Bonnier, General features of low energy $K\pi$ scattering from physical region method, Phys. Lett. B **46B**, 403 (1973).
[42] F. P. Palou, J. L. Sanchez Gomez, and F. J. Yndurain, Low-energy parameters for scattering of pions and kaons, Z. Phys. A **274**, 161 (1975).
[43] F. P. Palou and F. J. Yndurain, Low-energy $\pi\pi$ scattering parameters, Nuovo Cimento Soc. Ital. Fis. **19A**, 245 (1974).
[44] R. Kaminski, J. R. Pelaez, and F. J. Yndurain, Pion-pion scattering amplitude. II. Improved analysis above $\bar{K}K$ threshold, Phys. Rev. D **74**, 014001 (2006); **74**, 079903(E) (2006).
[45] R. Kaminski, J. R. Pelaez, and F. J. Yndurain, Pion-pion scattering amplitude. III. Improving the analysis with forward dispersion relations and Roy equations, Phys. Rev. D **77**, 054015 (2008).
[46] D. Epifanov *et al.* (Belle Collaboration), Study of $\tau^- \to K_S\pi^-\nu_\tau$ decay at Belle, Phys. Lett. B **654**, 65 (2007).
[47] V. Bernard, First determination of $f_+(0)|V_{us}|$ from a combined analysis of $\tau \to K\pi\nu_\tau$ decay and πK scattering with constraints from $K_{\ell 3}$ decays, J. High Energy Phys. 06 (2014) 082.
[48] P. Masjuan and J. J. Sanz-Cillero, Padé approximants and resonance poles, Eur. Phys. J. C **73**, 2594 (2013); P. Masjuan, J. Ruiz de Elvira, and J. J. Sanz-Cillero, Precise determination of resonance pole parameters through Padé approximants, Phys. Rev. D **90**, 097901 (2014); I. Caprini, P. Masjuan, J. Ruiz de Elvira, and J. J. Sanz-Cillero, On the uncertainty estimates of the σ-pole determination by Padé approximants, Phys. Rev. D **93**, 076004 (2016); I. Caprini, Finding the σ pole by analytic extrapolation of $\pi\pi$ scattering data, Phys. Rev. D **77**, 114019 (2008).